Performance of a prototype for a large-aperture multipass Nd:glass laser for inertial confinement fusion

Bruno M. Van Wonterghem, John R. Murray, Jack H. Campbell, D. Ralph Speck, Charles E. Barker, Ian C. Smith, Donald F. Browning, and William C. Behrendt

The Beamlet is a single-beam prototype of future multibeam megajoule-class Nd:glass laser drivers for inertial confinement fusion. It uses a multipass main amplifier, adaptive optics, and efficient, high-fluence frequency conversion to the third harmonic. The Beamlet amplifier contains Brewster-angle glass slabs with a clear aperture of 39 cm × 39 cm and a full-aperture plasma-electrode Pockels cell switch. It has been successfully tested over a range of pulse lengths from 1–10 ns up to energies at 1.053 μm of 5.8 kJ at 1 ns and 17.3 kJ at 10 ns. A 39-actuator deformable mirror corrects the beam quality to a Strehl ratio of as much as 0.4. The 1.053-μm output has been converted to the third harmonic at efficiencies as high as 80% and fluences as high as 8.7 J/cm^2 for 3-ns pulses.

Key words: Nd:glass laser, inertial confinement fusion, harmonic generation.

1. Introduction

The U.S. Department of Energy has established a project to design and construct a National Ignition Facility (NIF) for inertial confinement fusion (ICF) research.[1] The Commissariat a l'Energie Atomique of France has proposed building a *Laser Megajoule* of similar size and design.[2] Each of these facilities will contain a frequency-tripled, Nd:glass laser system capable of irradiating fusion targets at an energy of 1.8 MJ and power of 500 TW.

The output pulse shape and duration are flexible to satisfy a variety of applications, but the pulse specified for the baseline fusion target has a low-irradiance leading foot with a length of 15–20 ns and a final high-irradiance pulse with a length of 3–4 ns that contains most of the energy. A recent review by Lindl[3] describes the target physics underlying the choice of driver characteristics for the facility.

The NIF laser will have 192 independent subapertures (beamlets), each with an amplifier that has a square clear aperture of 40 cm × 40 cm and an output beam area slightly smaller than the clear aperture. The NIF laser and facility design are discussed in detail in a conceptual design report.[1]

We have constructed and are now testing a physics prototype of a single beamlet of the proposed NIF laser. The purpose of these tests is to show that the previously untested features of the NIF laser design will perform as projected at full scale and that the laser is therefore ready for the final engineering design. The final dimensions and component arrangements for NIF will differ somewhat from the prototype, but the differences are sufficiently small that these tests can be used to demonstrate a performance essentially equivalent to that of a NIF beamlet.

This paper summarizes the results of the first year of integrated tests of the prototypical NIF beamlet (called the Beamlet). Detailed design and test results for the oscillator, pulse shaping, preamplifier section,[4] the plasma-electrode Pockels cell switch,[5,6] the main amplifier,[7] the pulsed-power system,[8] and tests of some variations in laser architecture[9] are published elsewhere.

2. National Ignition Facility Laser Design Compared with Current Inertial Confinement Fusion Lasers

In this section we briefly review the differences between the NIF laser design and typical large Nd:glass lasers that are currently operating. In addition we also highlight the new features of the NIF design that are tested with the Beamlet.

The authors are with Lawrence Livermore National Laboratory, University of California, P.O. Box 808, Livermore, California 94551.

Received 3 September 1996; revised manuscript received 3 December 1996.

0003-6935/97/214932-22$10.00/0

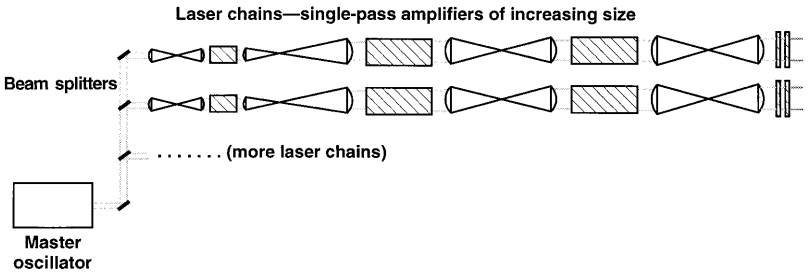

Fig. 1. Single-pass MOPA laser architecture commonly used in existing ICF lasers.

A. Current Inertial Confinement Fusion Laser Design: A Single-Pass Master-Oscillator, Power-Amplifier Architecture

Most large glass lasers designed for inertial fusion experiments have the single-pass master oscillator, power-amplifier (MOPA) architecture (Fig. 1): For example, the Nova laser[10–12] at Lawrence Livermore National Laboratory, U.S.A.; the Omega laser[13] at the Laboratory for Laser Energetics, University of Rochester, U.S.A.; the Gekko XII laser[14] at the Institute of Laser Engineering, University of Osaka, Japan; the Phébus laser[15] at the Commissariat a l'Énergie Atomique, Centre d'Études de Limeil-Valenton, France; and the Helen laser[16] at the Atomic Weapons Research Establishment, England, are all based on a single-pass MOPA design.

In the single-pass MOPA architecture a master oscillator generates a few nanoseconds pulse of several millijoules that is then spatially and temporally shaped at approximately a 1-cm aperture and split into parallel chains of single-pass rod and Brewster-angle slab amplifiers of increasing size. Gain isolation is provided at a small aperture ($<\sim$10 cm) by ring-electrode Pockels cells and thin-film polarizers. Faraday rotators, driven by pulsed electromagnets, are used at large apertures to isolate pulses from propagating backward down the laser chain. Single-beam amplifiers with round apertures as large as $\sim$32 cm are used in all these facilities. In addition, the Nova and the Phébus lasers have amplifiers with 46-cm apertures that use glass slabs that are split into two independent pieces.

The amplifier stages are separated by relay telescopes or spatial filters that reimage a beam-forming aperture at several places through the amplifier chain. This reimaging reduces the diffractive growth of spatial irradiance noise and provides Fourier-transform planes at the focal planes in the telescopes in which high-spatial-frequency irradiance noise can be reset to zero. The noise level needs to be kept low because nonlinear propagation effects cause it to grow exponentially at high irradiance.[17,18]

The single-pass MOPA is a familiar and well-proved design that can be assembled and tested in stages, so performance risk is low. Cost and complexity are high, however, because of the large number and variety of components required for a single-pass MOPA design. The Nova laser, for example, contains one rod amplifier and five sizes of elliptically shaped slab amplifiers (a total of 41 slabs) in each of ten laser chains.[10] There are also eight additional rod amplifiers of several sizes between the oscillator and the chains. In addition, there are relay telescopes and isolators between all these amplifier stages.[17]

B. Beamlet: A Large-Aperture, Multipass Laser Design

Current large ICF lasers were designed to operate with pulses of $\sim$1 ns or less. The larger NIF targets will require longer drive pulses, typically in the 3–5-ns range. The laser damage threshold of optical components at this longer pulse length is high enough that a major fraction of the energy stored in the amplifier can be extracted during the pulse. Because the gain of the amplifier is proportional to stored fluence, the last photon in the pulse will then see a much lower gain than that of the early photons, and the pulse distortion caused by this gain saturation becomes important to the design. Single-pass MOPA designs are particularly sensitive to this effect, because in order to minimize the cost of the preamplifiers they are made significantly smaller than the main final amplifier. This results in significant gain saturation in these early stages for high-fluence pulses, and the total pulse distortion, which is the product of the distortion in each of the saturating amplifiers, becomes severe.

A multipass amplifier uses the full aperture of the main amplifier as a preamplifier on early passes, and the fluence in these early passes never rises high enough to cause significant energy extraction or pulse distortion. Therefore the pulse distortion is limited to the distortion from the fluence extracted from the final pass through the amplifier. The multipass amplifier has the additional advantage of not requiring many intermediate preamplifiers, thus reducing costs. These features make multipass amplifiers desirable for the next generation of large ICF lasers. Optical distortions can add coherently in the multiple passes, however, and must be considered carefully in the design.

A multipass amplifier requires a method for separating input and output beams in the amplifier, which is not necessary in a single-pass system. There are three generic techniques for accomplishing this (Fig. 2): (1) A polarization rotator can be used to separate beams at a polarizer, (2) the beams can be separated in angle in the near field, or (3) they can be separated in angle in the far field near a focal plane. Near-field angle separation has been used with large

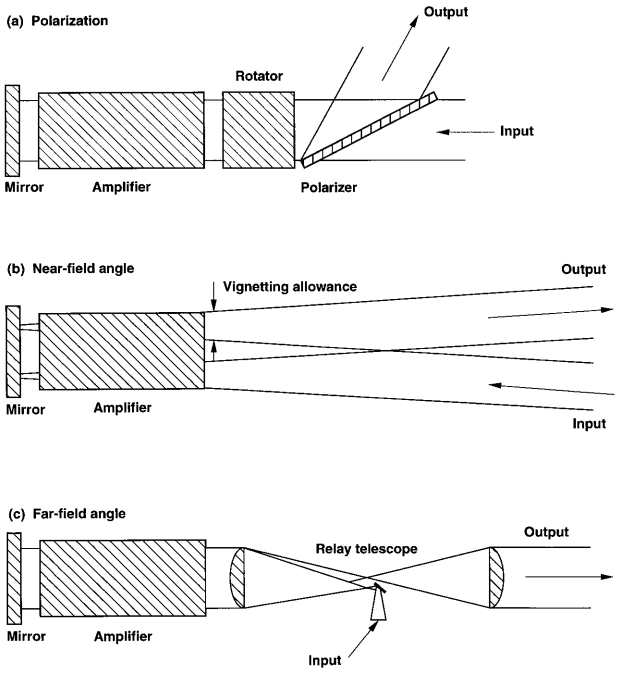

Fig. 2. Three generic schemes for separating the input and the output beams for a multipass laser architecture: (a) polarization rotator and polarizer, (b) near-field angle separation, (c) far-field angle separation. The NIF and the prototype Beamlet use a combination of far-field angle separation and polarization rotation.

laser systems.[19] It requires either a long propagation distance, leading to difficulties with diffraction, or a beam size much smaller than the amplifier aperture to accommodate the beam motion, leading to poor utilization of the amplifier volume. Therefore near-field separation has not been considered for the NIF design.

Far-field angle separation has several desirable features for this application. There is no closed path in the laser cavity, so parasitic oscillations are less of an issue than for a configuration in which there are closed resonant feedback paths. Each pass through the focal plane goes through a separate aperture in that plane, so the propagation of later passes is not affected by plasma generated in the aperture by earlier passes. Any leakage out of the cavity on early passes is at an angle to the final output beam, so it is easily occluded in a transport spatial filter and cannot disturb the laser target. Finally, far-field angular separation gives a convenient location for injecting a low-energy input pulse near the focal plane without requiring additional full-aperture optical components.

The Beamlet test series presented here uses a combination of far-field angle plus polarization separation. Polarization separation is achieved with a Pockels cell and a polarizer with apertures slightly larger than the beam in the main amplifier stage. The far-field angle separation gives the advantages just mentioned; the Pockels cell gives gain isolation and isolation from backreflections. The full-aperture Pockels cell also allows the off-axis angle in the far field to be very small because the energy handled on the injection optics is only ~1 J. The small angle allows efficient use of the amplifier aperture with a relatively short laser cavity. It is possible to configure the system to do separation in far-field angle only, with a smaller Pockels cell used for isolation and time gating. This alternative configuration requires handling the beam near the far field at energies up to 100 J, but avoids the cost of the full-aperture Pockels cell and polarizer. The Beamlet hardware is designed so that either configuration can be installed, and preliminary tests of this alternative configuration have been presented elsewhere.[9]

Figure 3 shows the multipass architecture used for the Beamlet laser design. The pulse-forming system uses a low-power oscillator whose output is injected into a single-mode optical fiber. The output from the fiber goes to a pulse-shaping system that uses waveguide modulators derived from the designs used in high-speed fiber communications networks, so that energy injection and pulse shaping are under direct, low-voltage computer control. The pulse output from the modulator is then fed to a single-mode, regenerative amplifier that amplifies the pulse to ~10 mJ.[4] A beam-shaping section forms the appropriate spatial irradiance profile that is injected into the preamplifier section of the laser. A four-pass, single-rod preamplifier increases the pulse to ~1 J and injects it near the focal plane of a spatial filter into the four-pass main amplifier. The pulse then passes four times through the large-aperture (nominally 39 cm × 39 cm) multipass amplifier cavity and reaches an energy of ~6 kJ. We choose four passes

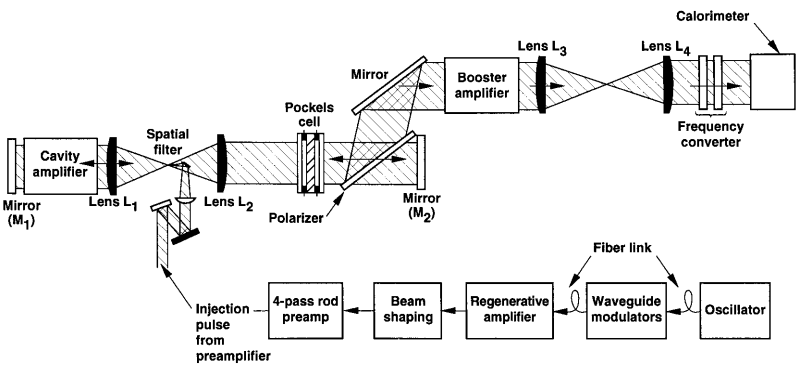

Fig. 3. Schematic layout of the multipass prototype Beamlet.

as a compromise among the size of the front end, the aperture loss that is due to off-axis propagation, and coherent addition of optical distortion. The 6-kJ pulse from the main cavity is then amplified by approximately a factor of 2 in the booster amplifier. Note that the amplifier is separated into two amplifier blocks (main and booster) to reduce the effects of nonlinear phase shift in the glass for pulses of high peak power. The output from the booster propagates to a frequency converter and, in the case of the NIF, to the target chamber.

The NIF laser design groups the main amplifiers into large arrays composed of apertures stacked two wide and four high. Six of these 4×2 units are close packed together to form a 12-wide, 4-high block of beamlets. These compact assemblies minimize the number of components and flash lamps and the building volume. The individual beamlets are optically independent, although supported by common mechanical hardware and pumped by common flash lamps. This full array of 48 apertures is too large and expensive to test in a small scientific prototyping effort. Therefore on the Beamlet we constructed the amplifier as an array of four apertures stacked two high and two wide to study many of the major issues of this type of amplifier assembly[7] (Fig. 4). Only one of the four Beamlet apertures contains high-quality laser glass; the other three apertures contain a low-cost glass whose absorption characteristics are similar to those of the laser glass. In this way we can simulate the pumping characteristics of a multiaperture amplifier array while using only one active beam line.

A pulsed-power system provides power to the flash lamps pumping the four apertures of the cavity and booster amplifiers. As shown in Fig. 4, the flash lamps are positioned in vertical arrays along the sides and in the midplane of the 2×2 amplifier module.[7] A preionization system triggers the flash lamps by delivering roughly 10% of the capacitor energy 200 μs before the main discharge. This improves the amplifier pump efficiency by approximately 5% and increases the lifetime of the flash lamps. The capacitor bank uses novel self-healing metallized film capacitors with a 10,000-shot rated lifetime and a stored energy density of ~ 1 J/cm^3 at the Beamlet operating voltage.

The Beamlet laser uses a distribution of 11 amplifier slabs in the cavity and five in the booster section. The amplifier sections are constrained to have an odd number of slabs, as this cancels asymmetric gain gradients in the two end slabs.[7]

An adaptive wave-front control system is used on the Beamlet to correct for static and dynamic optical aberrations. To our knowledge this is the first time such a system has been used on an ICF laser system. The Beamlet adaptive optics system consists of a 39-actuator deformable mirror (DFM), two Hartmann wave-front sensors, and a closed-loop controller. This adaptive optics technology was developed and demonstrated on large dye laser systems used for isotope separation.[20]

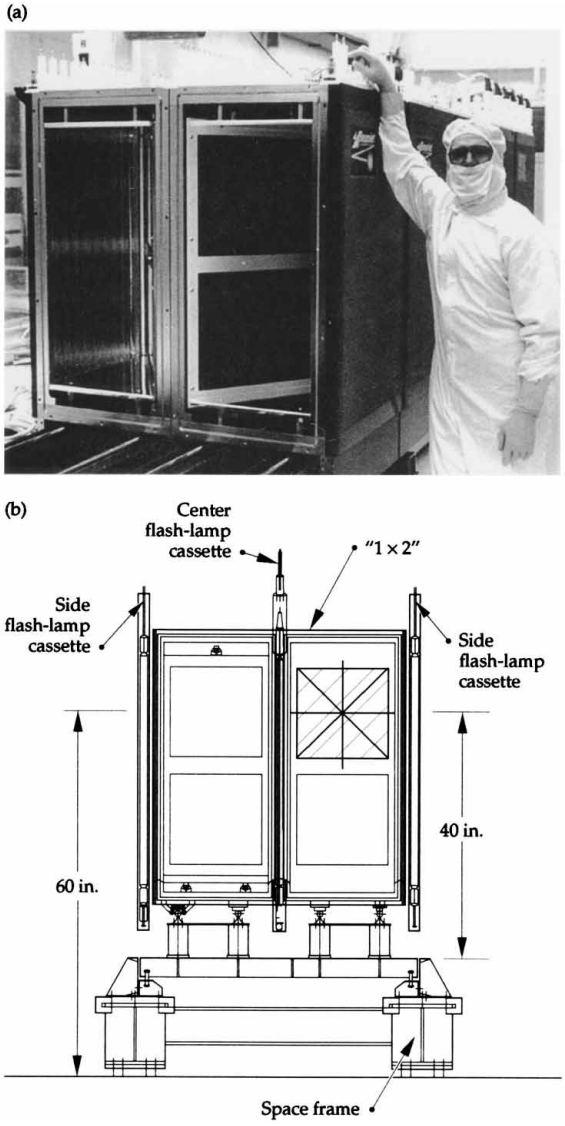

Fig. 4. (a) Photograph of assembled 2×2 Beamlet amplifiers with 39.5 cm $\times$ 39.5 cm, hard-edged apertures (this supports approximately a 35 cm $\times$ 35 cm beam size), (b) schematic drawing showing key elements of the design; the top right-hand square is the active beam aperture.

3. Test Configuration of the Beamlet Laser

Figures 5 and 6 show a plan view and a photograph of the Beamlet laser system as configured for the test series presented here. The Beamlet is constructed on top of a 1-m-thick reinforced concrete floor that serves as an optical bench.

We use a prototype[4] of the pulse-generation and preamplifier system proposed for the NIF to produce an approximately 1-J pulse that is injected into the four-pass laser cavity. The output pulse from the front end is injected into the four-pass cavity by a small 2 cm $\times$ 2 cm 45° mirror (beam dimensions 1.3 cm $\times$ 1.3 cm), and the pulse comes to a focus at an aperture in the focal plane of a vacuum spatial filter. The pulse expands past focus to fill a recollimating lens and propagates through the multisegment am-

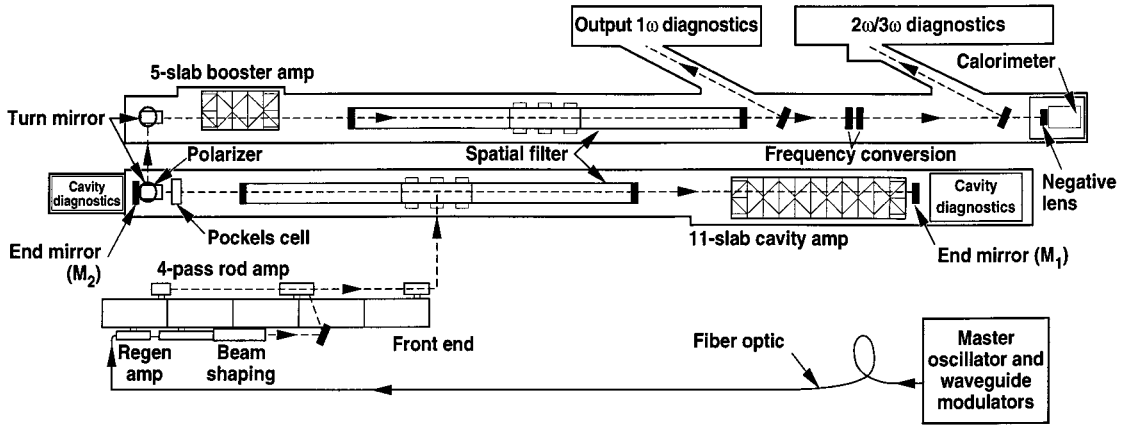

Fig. 5. Plan view of the Beamlet as configured for the tests described in this paper.

plifier stage containing the eleven Brewster-angle slabs. It then reflects from cavity end mirror M_1 and makes a second pass through the multipass amplifier, emerging with an energy of ~150 J.

At the other end of the laser cavity is an optical switch, consisting of a plasma-electrode Pockels cell and a polarizer.[5] As the pulse is injected for its first two passes through the multipass amplifier, the Pockels cell is switched on to rotate the polarization so that the pulse passes through the polarizer and strikes a second mirror, M_2 (Fig. 5). It then returns to the multipass amplifier for a third and fourth pass, emerging with an energy near 6 kJ. By the time it returns to the Pockels cell, the cell has switched off, so the pulse then reflects from the polarizer and makes a single pass through the booster amplifier containing five Brewster-angle slabs. A transport spatial filter relays the pulse to the frequency converter. At this point, the 1.05-μm energy is ~12 kJ.

The Beamlet, like other large ICF lasers, is an image-relayed system. A beam-forming aperture in the preamplifier shapes the beam to be injected into the main laser amplifier. The optics are designed so that images of that aperture lie in the planes of laser cavity mirrors M_1 and M_2, which are separated by 36 m, or four times the 9-m focal length of lenses L_1 and L_2. The transport spatial filter (L_3 and L_4) forms an image of this relay plane on the frequency converters. The diffractive propagation distance goes to zero at these images, so there is reduced amplitude modulation near these planes.

Figure 7 is a schematic of the array of pinhole apertures at the focal plane of the cavity spatial filter. Mirror M_1 is positioned such that the pulse injected through pinhole 1 returns to a position at pinhole 2. Similarly, mirror M_2 is aligned so that it reflects the beam to pinhole position 3. The return from the second pass then automatically lies at pinhole 4. Any energy not switched out of the cavity strikes mirror M_2 and returns to the focal plane at position 5, where it is intercepted by an absorbing glass beam dump. For this series of experiments, we used 3.6-mm-diameter pinhole apertures, giving a spatial cutoff wavelength of 5.3 mm in the near field or an

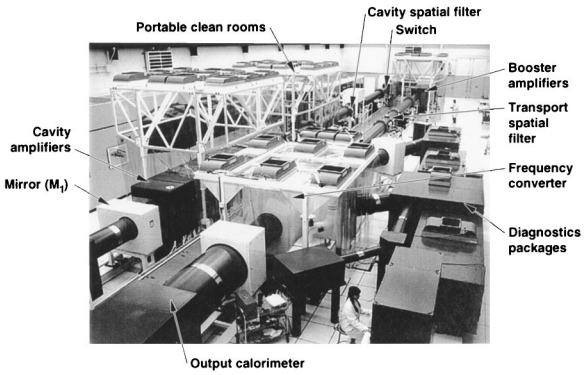

Fig. 6. Photograph of the fully assembled Beamlet prototype laser. The laser is housed in a nominally class 10,000 clean room whose temperature is controlled to approximately ±1 K. Portable clean rooms providing class 100 cleanliness levels can be positioned anywhere within the system.

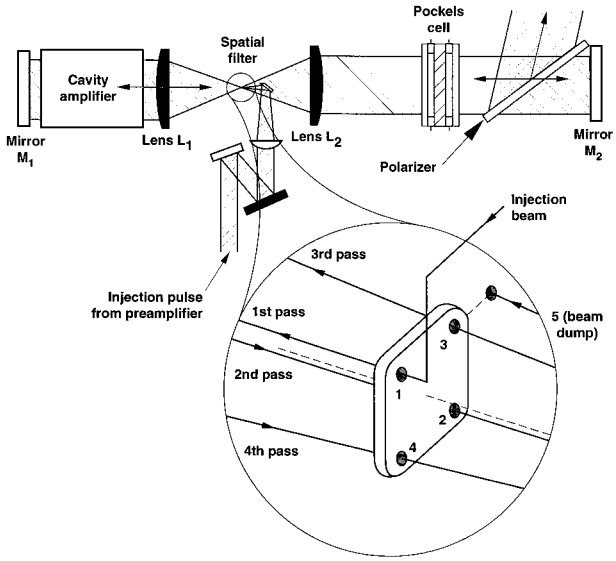

Fig. 7. Pinhole-array layout at the focal plane of the Beamlet multipass cavity.

Table 1. Laser Damage Thresholds and Maximum Safe Operating Fluences for the Beamlet Optics[a]

Material	Measured Small-Spot Damage Thresholds		Safety Factor	Maximum Safe Operating Fluence	
	1.06 μm (J/cm^2)	0.351 μm (J/cm^2)		1.06 μm (J/cm^2)	0.351 μm (J/cm^2)
Fused silica (surface)	$22t_p^{0.4}$	$9t_p^{0.5}$	0.8	$18t_p^{0.4}$	$7t_p^{0.5}$
Laser glass (surface)	$22t_p^{0.4}$	—	0.8	$18t_p^{0.4}$	—
HfO_2/SiO_2 coatings					
mirror	$19t_p^{0.3}$	—	0.7	$13t_p^{0.3}$	—
polarizer (p polarization)	$14t_p^{0.3}$	—	0.7	$10t_p^{0.3}$	—
polarizer (s polarization)	$16t_p^{0.3}$	—	0.7	$11t_p^{0.3}$	—
SiO_2 solgel	$\sim 22t_p^{0.4}$	$10t_p^{0.4}$	0.85	$19t_p^{0.4}$	$8.5t_p^{0.4}$
KDP (bulk)	$20t_p^{0.5}$	$9t_p^{0.5}$	0.7	$14t_p^{0.4}$	$6.5t_p^{0.5}$

[a]The data include the measured pulse-length dependence, where t_p is the pulse length in nanoseconds.

angular acceptance of ±200 μrad in the far field. The pinhole apertures are arranged in a square array with 3-cm separation between pinholes.

The clear aperture of the potassium dihydrogen phosphate (KDP) crystal installed in the Pockels cell is 37 cm, which sets a beam hard aperture of ~35 cm. The beam must be smaller than the smallest clear aperture because of the vignetting allowance for beam motion that is due to off-axis propagation plus an allowance for alignment. The 39-cm amplifier aperture is not completely filled under these conditions and could support slightly larger beam dimensions.

The beam is reflected out of the multipass cavity by the polarizer and then routed to the booster amplifier by three turning mirrors (see Fig. 5). After passing through a second spatial filter that has the same image-relay characteristics and pinhole size as the one in the multipass cavity, the beam passes through a fused-silica beam splitter. The beam splitter reflects a small portion of the 1-μm output beam to a diagnostics package. This package captures near- and far-field images on charge-coupled-device (CCD) cameras, determines the energy with a calorimeter, and measures the temporal pulse shape with a vacuum photodiode with a transient digitizer or a streak camera. It also includes a 77-element CCD-based Hartmann sensor to measure wave-front distortion and to control the figure of the 39-actuator DFM.

The 1.053-μm output beam enters a dual-crystal frequency converter. The frequency converter uses a type I/II third-harmonic generation scheme, consisting of a 1.05-cm-thick KDP doubler crystal and a 0.95-cm-thick, 80% deuterated, KD*P tripler crystal. In the experiments described here, both 32 cm × 32 cm and 37 cm × 37 cm crystals were used; these crystals will convert beams up to 30 and 34.5 cm in size. (Further details of the harmonic converter are given in Section 6.) Finally, the output beam is absorbed by a 74 cm × 74 cm calorimeter/beam dump after first passing through a negative lens. The beam expansion reduces the fluence below the damage threshold of the absorbing glass in the calorimeter.

4. Key Optical Materials and Damage Threshold Limits

Many of the optics used on the beamlet are larger and have higher damage thresholds than those used on previous ICF lasers; details of the optics are described elsewhere.[21] Perhaps the most critical characteristic of the optics is the damage threshold. Table 1 summarizes the off-line measured damage thresholds for the Beamlet optics. Note that these measured thresholds represent the absolute maximum operating fluences possible for that specific optical material. We keep peak fluences 15%–30% below these thresholds to provide an operational margin of safety.

Our greatest concern for optical damage was at the large polarizer in the laser cavity and the KD*P third-harmonic crystal. The polarizer HfO_2/SiO_2 thin-film coating was deposited on a 75 cm × 39 cm × 9 cm BK-7 substrate. HfO_2/SiO_2 multilayer coatings were used because of their demonstrated damage threshold improvement with laser conditioning.[22] The polarizer extinction coefficient was >700, and the measured conditioned damage threshold for both s- and p-polarized light is >18 J/cm^2 at 3 ns and 1054 nm.

Large plates of single-crystal KDP are used in the Beamlet Pockels cell and frequency converter. The Pockels cell and second-harmonic generation crystals are undeuterated, whereas the tripling crystal is deuterated to a level of ~80%. These crystals were cut from solution-grown single-crystal boules of KDP and KD*P weighing as much as 500 kg each. The plates cut from these boules were then diamond turned to a surface smoothness of ~40–140 Å rms (recent improvements in KDP diamond turning have reduced the surface roughness to 20–50 Å rms). The crystals were laser conditioned[23] on line by a slow increase in the incident fluence. Off-line tests show that conditioning increases the 1054-nm damage threshold from 34 to 43 J/cm^2 at 3 ns for the KDP Pockels cell and doubler crystals. Similar off-line tests show that conditioning the 80% deuterated tripler crystal increases the 1054-nm threshold from 16 to 25 J/cm^2 and the 351-nm threshold from 10 to 20 J/cm^2 at 3 ns.

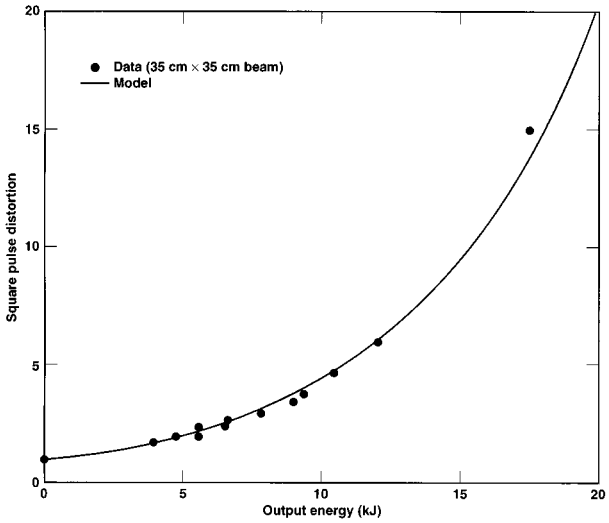

Fig. 8. Comparison of the measured and the calculated temporal square-pulse distortions versus output energy at 1.05 μm.

5. Measurement of the Beamlet Laser Performance at 1.05 μm

A. Temporal Pulse Shaping and Bandwidth

All performance results presented here are for pulses temporally shaped to give amplified output pulses with a flattop temporal profile. To compensate for the gain saturation in the amplifier, injected pulses are exponentially shaped with a contrast that is dependent on the output fluence. An integrated optical waveguide modulator, driven by low-voltage pulse generators, provides shaped pulses with a contrast of as high as 100 and rise times below 75 ps. The pulse contrast is defined as the ratio of power at the end of the pulse to the power at the beginning of the pulse. Figure 8 shows the input contrast required as a function of output fluence to maintain a square output pulse.

The input pulse is also phase modulated at a frequency of 5 GHz to a bandwidth of 30 GHz. This added bandwidth is required[24–26] for preventing transverse stimulated Brillouin scattering (SBS) in the optical components at the output of the system. This bandwidth is adequate to suppress SBS under all conditions tested, the most severe being at the third harmonic. Phase modulation is generated by the application of a low-power rf signal to a longitudinal phase modulator, which is an integral part of the same integrated optical circuit used for temporal pulse shaping.

B. Optical Transmission of the Laser System

Optical losses can reduce the laser output, particularly with long pulses for which the laser amplifiers are highly saturated. It is important to quantify these losses in order to compare the measured laser output with theoretical models.

We measured the 1.05-μm transmission through the entire beamlet system and from one spatial filter pinhole to the next. During all the measurements the amplifiers were unpumped. The total transmission from injection to output through 148 optical surfaces is 43% and agrees with a calculation based on component transmission losses shown in Table 2.

Table 2. Optical Transmission Data for the Beamlet Amplifier Components

Component	Transmission at 1.05 μm
LG-750 laser glass at Brewster's angle	0.995
Solgel AR coating	0.995
KDP switch crystal	0.934
Polarizer transmission (p polarization)	0.974
Polarizer reflection (s polarization)	0.989
Multilayer dielectric mirror	0.99

The major contributors to the 1.05-μm transmission losses in the laser system are (1) laser slabs, (2) the optical switch (Pockels cell plus polarizer), (3) high-reflectivity mirrors, and (4) solgel antireflection (AR) coatings. To quantify these losses, we conducted both on-line and off-line measurements of the transmission of individual optical components. The average amplifier slab transmission loss determined from system transmission measurements is 99.45%. This agrees well with absorption measurements carried out on individual slabs, which gives transmission values ranging from 99.3% to 99.6%, with an average value of 99.5%. Note that these measurements include the loss in the unpumped glass that is due to the Nd ions that thermally populate the $^4I_{11/2}$ terminal laser level. This loss, which we estimate to be $\sim 6 \times 10^{-4}$ cm^{-1} for a 3.5×10^{20}/cm^3 doping level,[27] becomes negligible during flash-lamp pumping.

The double-pass transmission through the optical switch (i.e., the Pockels cell plus polarizer) is 71%. The 1-cm-thick undeuterated KDP crystal has an absorption loss[28,29] of 6%/cm at 1.05 μm and thus is the major contributor to the switch loss. In addition the measured single-pass transmission through the polarizer for p-polarized light is 97.3%; this comprises a 1.1% loss through the 9-cm-thick BK-7 substrate plus a 1.5% loss associated with the dielectric thin-film coating.

On a typical high-power laser shot (output energy of 12 kJ), nearly 6 kJ of energy are extracted from the multipass cavity, and the energy lost through the polarizer (which is due to s-polarized leakage plus any light rotated to p polarization by birefringence in the system) is less than 30 J, as measured by a diagnostics package at the end of the multipass cavity. This loss results mainly from strain birefringence in the vacuum windows of the Pockels cell.[5]

The thin-film optics used on the beamlet all have low losses. Freshly deposited solgel AR coatings have a transmission of 0.995. We occasionally observe increased losses in AR coatings on the vacuum side of fused-silica spatial filter lenses, as a consequence of contamination by outgassing products (notably hydrocarbons) or possibly material ablated from the pinhole. The high-reflectivity, dielectric

thin-film mirrors that are used at the ends of the cavity and in the beam-transport section of the laser have an aperture average reflectivity of ≥99% at 1.05 μm.

C. Edge Apodization and Fill Factor

It is important to have a flat output profile with a maximum aperture fill factor to maximize the output energy of the system. To achieve this, we compensate for nonuniform gain in the amplifiers and shape the beam's edges to minimize the rolloff area along the perimeter while minimizing diffractive edge modulation growth.

A 1-cm margin around the edge of a nominal 34 cm × 34 cm beam contains 11% of the beam area, so changes of only a few millimeters in beam dimensions can have a noticeable effect on the output energy of the system. Edge diffraction from sharp beam edges causes irradiance peaks on the beam, however, so the beam irradiance at the edge must be apodized (that is, the irradiance must decrease smoothly to zero over a region occupying at least a few Fresnel zones over the propagation distances for which these irradiance peaks are not acceptable). The edge profile is created by use of a precision serrated aperture.[30] The shape of the serrations determines the edge profile, after the high spatial frequencies from individual serrations are removed by a spatial filter.

The edge apodization used in most of the data presented here is an inverted Gaussian profile with the 10^{-2} irradiance point defined as the hard aperture of the beam. This is considered the zero-irradiance level that is allowed to strike the edges of the clear aperture of optical components. When this dimension is set to 34 cm, the half-power points are separated by 31.2 cm and the peak of the Gaussian profile joins the flattop central area at 27.2 cm. The corners of the beam are rounded with a radius of 5 cm to suppress diffraction from the corner, which subtracts 20 cm^2 from the beam area. When the beam is set to a different size (to accommodate frequency-conversion crystals that have a clear aperture of 30 cm, as an example), these dimensions scale proportionally. The tests reported here used beams with sizes ranging between 29.5 and 35 cm.

The experimental data show no growth of diffractive irradiance peaks around the edge of the beam, although propagation simulations suggest that there is some growth under high-fluence and high-nonlinear-phase-shift conditions near the end of the pulse. The effective beam area at half power is 971 cm^2 after allowing for the 20 cm^2 loss in the corners. The fill factor, defined as the ratio of the beam energy to the energy if the entire 34 cm × 34 cm square hard aperture were filled at the fluence of the flat central area of the beam, is 84%.

Recently we reduced the apodization border (from hard edge to half-power point) on each side of the aperture from 1.4 to 0.85 cm, giving a larger fill factor of 86%. At low power, the irradiance modulation induced by the sharper edge is less than the typical random irradiance noise on the beam. High-power experiments will verify limits to further reduction in the apodization border.

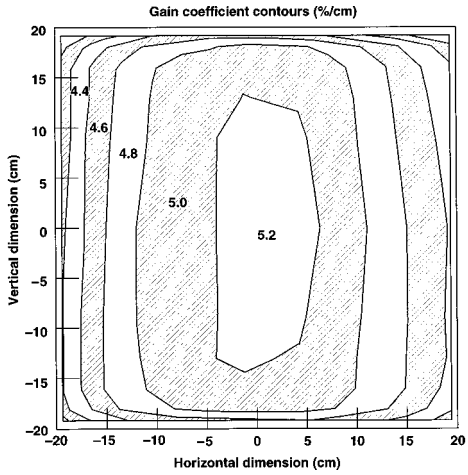

Fig. 9. Gain profile for a five-slab-long amplifier. Amplified spontaneous emission causes the gain to roll off near the edges in the horizontal direction of the slab.

D. Compensation for Amplifier Gain Nonuniformity

Figure 9 shows the gain profile of a five-slab-long Beamlet amplifier pumped to its nominal operating point. The gain peaks in the center of the aperture and is ~15% lower in the extreme corners of the aperture. Most of the gain rolloff is in the horizontal direction, which is the long dimension of the Brewster-angle slab. Amplified spontaneous emission trapped by total internal reflection within the slabs depletes the stored energy near the slab edges that are perpendicular to the long axis of the glass and causes this gain rolloff. The combined effect of propagation through 49 slabs leads to a significant spatial gain profile variation. Therefore, to achieve a flat output profile, we must shape the input irradiance profile to the final multipass amplifier stage to compensate for the nonuniform gain profile in the horizontal direction (the effect of the vertical gain profile is insignificant). The input profile used for the results presented in this paper is a parabolic irradiance profile in the horizontal direction with the edges of the aperture twice as intense as the center (Fig. 10). A vacuum-deposited Al transmission filter with a parabolic transmission profile is used for this purpose. Gain compensation is most important for short pulses at low extraction efficiency, where much of the gain is exponential. In highly saturated operation with long pulses, the gain profile is less important.

E. Energy Performance

Figure 11 shows the Beamlet output energy as a function of input energy to the four-pass amplifier for a hard aperture of 35 cm × 35 cm and with the improved fill factor of 87%. The solid curve is the predicted performance from a model that includes measured gains and optical transmissions of the sys-

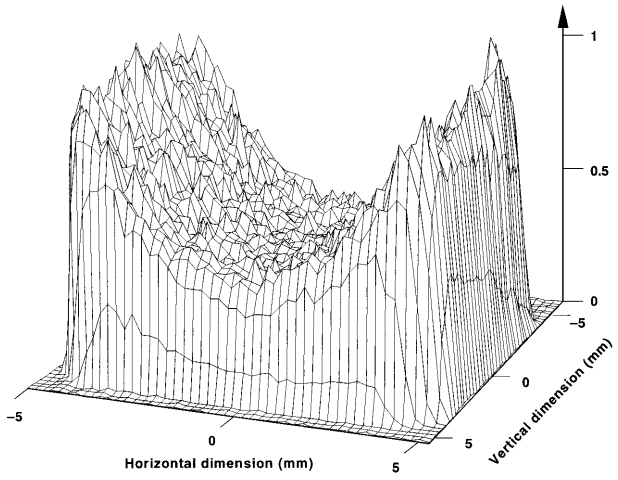

Fig. 10. Two-dimensional plot of the measured parabolic beam profile injected into the main amplifier cavity.

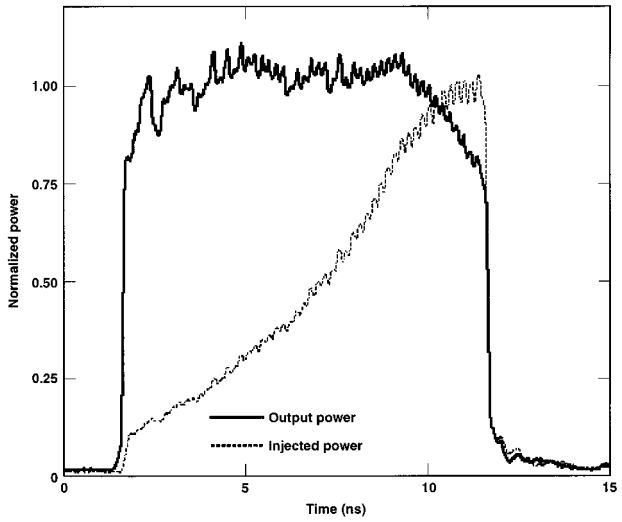

Fig. 12. Comparison of temporal shapes of the injected and output pulses. The 5-GHz phase modulation causes the amplitude modulation seen on the pulse shape.

tem. The aperture-averaged small-signal gain is $\sim 6.8 \times 10^4$ for a 35-cm beam size.

The energy transfer function shown in Fig. 11 does not depend on the temporal pulse shape; however, the input pulses for the shots plotted here were shaped to give square output pulses, as discussed above. Figure 12 shows an example of input and output temporal pulse shapes under highly saturated conditions with a 1.053-μm output energy of 17.3 kJ at 10 ns. A partial conversion of phase to amplitude modulation within the front end is visible on this shot. Note also that in this particular shot the input contrast was not set quite high enough to obtain a flat output profile past 8 ns. Figure 8 shows the contrast that is required for compensating for gain saturation versus output energy for a 35-cm beam.

The safe operating limits for a large glass laser are set by surface or bulk damage to optical components, as discussed above.[31] High irradiance also causes nonlinear growth of amplitude noise on the beam, which leads to higher local fluence and hence damage at lower average fluence. The safe operating range is most conveniently displayed in fluence–irradiance space, as shown by the region under the solid curve in Fig. 13. For short pulses ($<\sim 3$ ns), the safe operating limit is set by nonlinear growth of irradiance structure through the Pockels cell and booster amplifier that then leads to a risk of damage at lens L_3 (see Fig. 3). Intermediate pulse lengths (~ 3–8 ns) are limited by damage to the polarizer or by damage at lens L_1 caused by nonlinear amplitude growth through the main cavity amplifier. Long pulses ($>\sim 5$–8 ns) are limited less by damage than by depletion of the stored energy in the amplifier. This practical limit is reached when the gain in the amplifier falls to such a low value that it is impractical

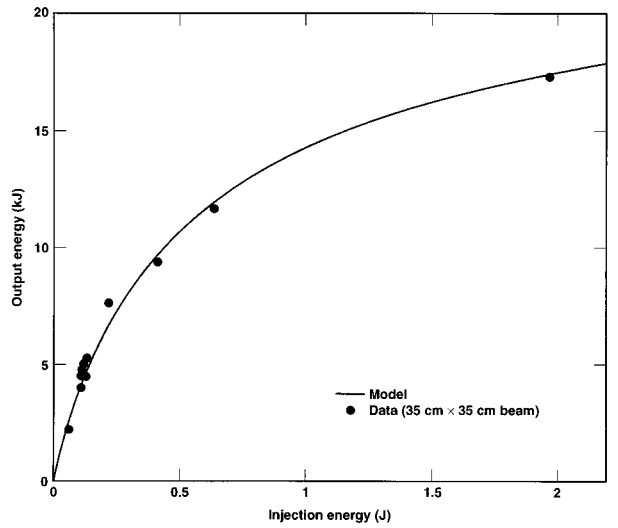

Fig. 11. Measured and predicted Beamlet output energies at 1.05 μm versus energy of the pulse injected into the multipass cavity.

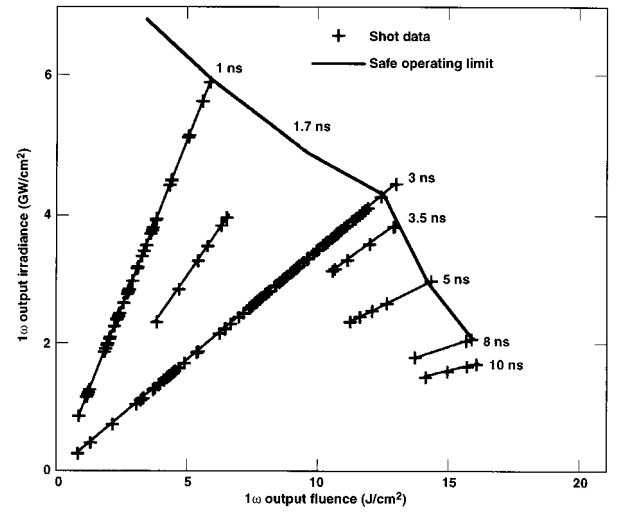

Fig. 13. Beamlet shot data plotted in 1ω irradiance versus fluence space. The region below the solid curve represents the safe operating region.

to maintain a square-output-pulse shape from the system. Fusion laser output pulses are generally peaked at or near the end of the pulse, so this square-pulse limit is appropriate for these pulses. A contrast ratio of 25 is usually considered to be a maximum practical value. We expect the Beamlet laser to operate safely with currently available components in the area to the left and below the boundary shown in Fig. 13.

We have fired roughly 550 full system shots on the Beamlet over the first 15 months of operation, and a number of these are plotted in Fig. 13. Each line on the figure represents shots at a particular pulse length. The maximum pulse duration on the Beamlet is limited to 10 ns by the round-trip time of the regenerative amplifier in the front end. Before conversion to the third harmonic, the nominal 1.053-μm output pulse for ICF ignition target experiments has an average fluence of 12 J/cm^2 and a peak irradiance of 3.3 GW/cm^2. Although the total duration of the shaped pulse is 15–20 ns, most of the energy is delivered in the last 3–3.5 ns.[1,3] A square, 5-ns pulse that has the same peak output irradiance and the same fluence as this shaped pulse has roughly the same nonlinear optical phase shift and damage threat to the system. The projected safe operating limit for the Beamlet is ~10% above these nominal operating conditions. We have fired ~50 shots at or above nominal NIF operating levels from 3 to 5 ns, including three shots slightly over the projected safe operating limit. Experiments in which fusion ignition is studied will usually require 3–5-ns pulses, but the NIF will also be used for other experiments requiring longer or shorter pulses. We have also operated up to the projected safe operating limit with pulses at 1, 8, and 10 ns.

F. 1.05-μm Beam Quality

1. Near-Field Beam Features

All large glass lasers have irradiance noise in the near field as a result of diffraction from small obscurations and flaws in the many optical components that the beam traverses. It is important to minimize the irradiance noise in large systems to reduce the peak irradiance so that we can have a higher average irradiance in the beam. Therefore it is important to understand the sources for these modulations in considerable detail.

Figure 14 shows a near-field image of the Beamlet output at ~6 kJ/3 ns from the multipass cavity alone (without the booster amplifier present). This image displays some of the irradiance modulation features that we could see on the beam exiting the multipass cavity when the laser was first activated. The peak-to-average modulation in this image is ~1.3:1 and shows several characteristic patterns for which the sources have been identified; these include (1) a set of circular arcs with a period of 6.4 mm, (2) a pattern of horizontal lines, (3) three black obscurations near the center of the image, and (4) Airy diffraction patterns.

The modulation that produces the circular arcs is

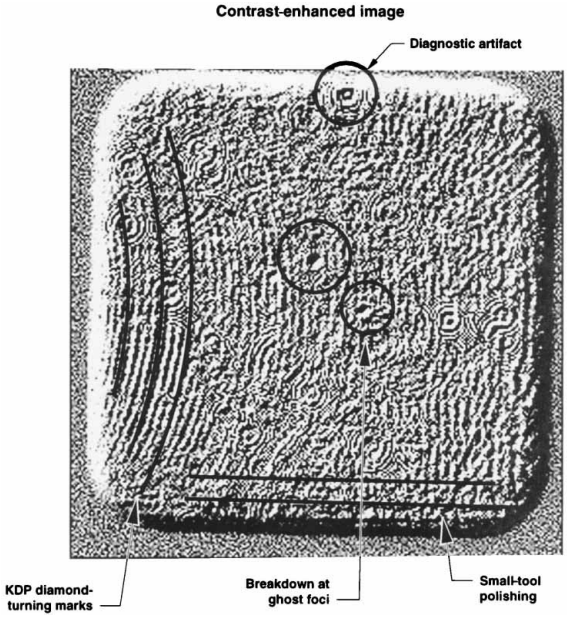

Fig. 14. Contrast-enhanced image of beam-fluence profile showing beam modulation (noise) caused by various effects, as discussed in the text.

from a periodic surface ripple imprinted on the surface of the KDP Pockels cell crystal. This surface ripple is generated during the diamond-turning process used to finish the crystal surface. The diamond-turning machine and procedures have been improved, based on this observation, and we now have a crystal installed on the system in which modulation caused by KDP surface features is much less visible. Further improvement to the diamond-turning process has made these features undetectable in recent test samples.

The major source of the horizontal lines is a residual surface ripple in the laser slabs that is an artifact of the raster-scan pattern of a small-tool polishing system used by an optical finisher. The amplitude of the surface ripples is very small—of the order of 1/100 wave or less for a typical slab—but can nevertheless lead to noticeable modulation. There were three slabs installed in the amplifier that were significantly worse than the typical slab when this image was recorded, so these ripples were also more apparent here than they are now after those slabs were replaced. Some irradiance features of this sort have also been traced to index variations in the laser glass, also of the order of 1/100 wave.

The three black obscurations in Fig. 14 originate from ghost reflections. Ghosts refer to reflections from nominally AR-coated surfaces. These occur throughout the laser system. A reflection of less than 1% for beam energies greater than ~100 J can easily be intense enough to cause optical breakdown or damage, particularly if it comes to a focus. The Beamlet is designed so that ghost reflections from cavity spatial filter lenses come to a focus in air between the lens and the amplifier or Pockels cell and cause small air breakdown plasmas to form. When the laser pulse returns through that region on a later

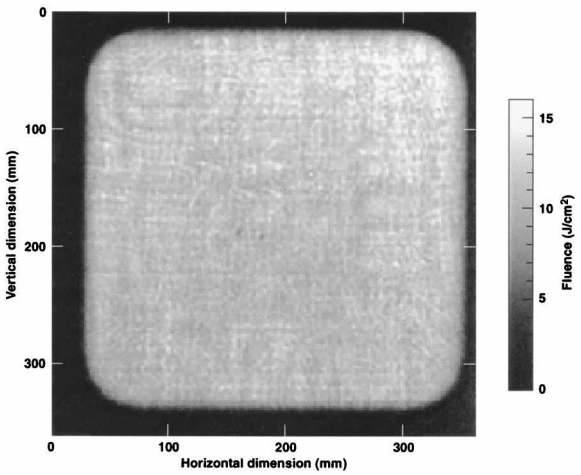

Fig. 15. Image of the beam-fluence profile showing the reduction in modulation after the optical finishing of several components in the laser beam line has been improved; compare with Fig. 14.

pass, these ghost foci appear as small obscurations on the beam. The obscurations are much less apparent after the booster amplifier, as they fill in because of unsaturated gain in that amplifier stage.

The Airy patterns seen on the beam image are caused by small opaque defects, typically dust particles or small bubbles in glass optical components. Some of these (including the large one so marked) are in the diagnostic camera system rather than in the laser itself.

Over the period of time since the Beamlet was first activated, we have worked to improve the quality of the optics to eliminate the source of the four features discussed above. Figure 15 shows a near-field image of the Beamlet output, including the booster amplifier after these improvements. Note that the modulations are much less apparent, although some minor modulations are still detectable.

Figure 16 shows a histogram of the fluence distribution in the output beam at the frequency converter under nominal operating conditions of 12 J/cm^2 in 3 ns. The camera pixel size is 0.7 mm $\times$ 0.7 mm when projected to the main beam aperture, although the optical resolution of the camera is slightly larger and explains why the measured distribution is slightly narrower than the modeled distribution[32] that is also shown in Fig. 16. The simulation includes optical phase aberrations measured for typical Beamlet optical components. The peak-to-average fluence ratio in the near field is typically 1.3:1 or less, as shown in this image.

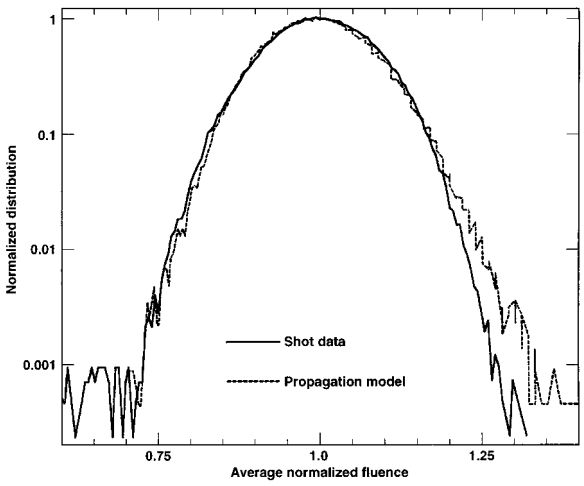

Fig. 16. Histogram of the measured and the calculated fluence distributions over the central area of the 1.05-μm output beam near-field image that is shown in Fig. 15.

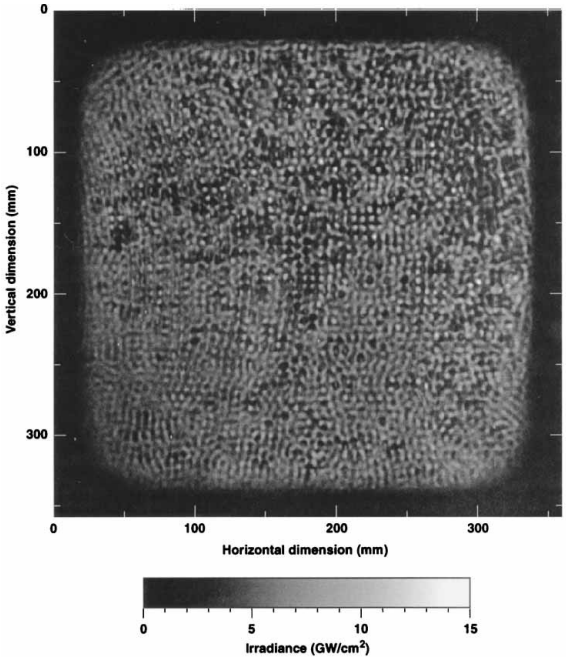

Fig. 17. Near-field image of the 1.053-μm output beam for a 5.5-GW/cm^2 shot at a 200-ps pulse width. The white dots are hot spots with an irradiance nearly five times the average irradiance.

2. *Nonlinear Effects at High Irradiance*

It is important to quantify the onset of beam breakup that is due to self-focusing caused by the nonlinear index of refraction in the optical components, because this effect limits the laser output irradiance for short pulses. Also it is important to test whether theoretical models correctly predict when beam breakup will set in. These studies can put the laser components at risk, as the irradiance modulation can grow quickly to damaging levels. To minimize the risk to the laser, we chose to study the growth of irradiance modulation at the end of a long pulse by studying a short (200-ps) pulse propagating through the laser with the booster amplifier unpumped. This simulates a condition in which all stored energy in the booster amplifier has been extracted by the earlier portion of a long pulse, and the laser glass slabs act merely as a series of nonlinear components that produce nonlinear phase push back and modulation growth, but no energy gain.

Figure 17 shows the near field of a beam at an

output irradiance of 5.5 GW/cm^2. The nonlinear phase shift accumulated through the Pockels cell and booster amplifier is 3.2 rad in this case, while the total phase shift through the amplifier chain exceeds 5.2 rad. Peak-to-average irradiance modulation in the output near-field image exceeds 5:1 and clearly indicates the onset of beam breakup by small-scale self-focusing. There was some filamentation in the last booster amplifier slab during this shot. This shot was taken with the original KDP Pockels cell crystal, which imposed a 6.4-mm period modulation on the beam, as shown in Fig. 14, and it is clear that this modulation serves as a seeding source for the nonlinear irradiance growth. The actual output energy is 20% below expected energy, indicating a significant amount of energy being lost, largely by clipping of high spatial frequencies on the final pinholes in the system ($\pm$200 μrad for this particular shot). Figure 18 shows the far-field distribution of the beam at 5.5 GW/cm^2. The $\pm$200-μrad cutoff angle of the spatial filter is visible as a faint circular shadow, confirming the presence of large-angle scattering.

Models predict[17,18] that the peak nonlinear gain in the system should be for spatial scales that map into ~150–250-μrad angle in the far field, and we see that there is significant growth around that angle. Operation at high irradiance will require cutoff angles in the spatial filters that are somewhat smaller than the $\pm$200-μrad cutoff used in the data presented here.

Figure 19 shows more recent results of modulation growth with an improved Pockels cell crystal. The modulation begins to grow noticeably through the booster amplifier at irradiances above 3 GW/cm^2 with $\pm$200-μrad cutoff in the cavity spatial filter, reaching 2:1 at ~4 GW/cm^2. If the high-spatial-frequency noise is cut off for angles greater than $\pm$150 μrad in the transport spatial filter, the modulation at 4 GW/cm^2 falls to ~1.3:1. These observations are consistent with propagation simulations for which a fast Fourier-transform optical propagation code is used and are discussed in a separate publication.[32]

3. *Beam Divergence and Wave-Front Control*

The nominal NIF ignition target design requires a 0.5-mm-diameter spot at the focus of a 7-m focal-length lens.[1,3] Energy lying much outside this $\pm$35-μrad angle is not useful and can be harmful if it strikes the wrong area of certain targets. Some experiments planned for NIF could use smaller spots, so a smaller beam divergence is desired. The diffraction limit (first zero of the Airy pattern) of a nominal 35-cm beam is $\pm$3.5 μrad, so a NIF beamlet should be better than 10 times the diffraction limit, as usually defined, at the fundamental 1053-nm wavelength.

Table 3 lists the typical magnitude, scale, and time variation of five major wave-front aberration sources that contribute to the beam divergence or wave-front quality at the output of a laser such as the Beamlet.

The first important source is the optical figure error, which is the large-scale or low-spatial-frequency departure of optical surfaces from their desired figure. A typical high-quality laser component will have an optical figure within $\lambda/10$ to $\lambda/4$ of the desired surface, but the cumulative effect of passing through many such components (76 passes through full-aperture components in the Beamlet between the injection mirror and the frequency converter) can be several waves. Mount-induced distortions and the gravity-induced sag of polarizers mounted as in the Beamlet must also be included.

The second major source is pump-induced distor-

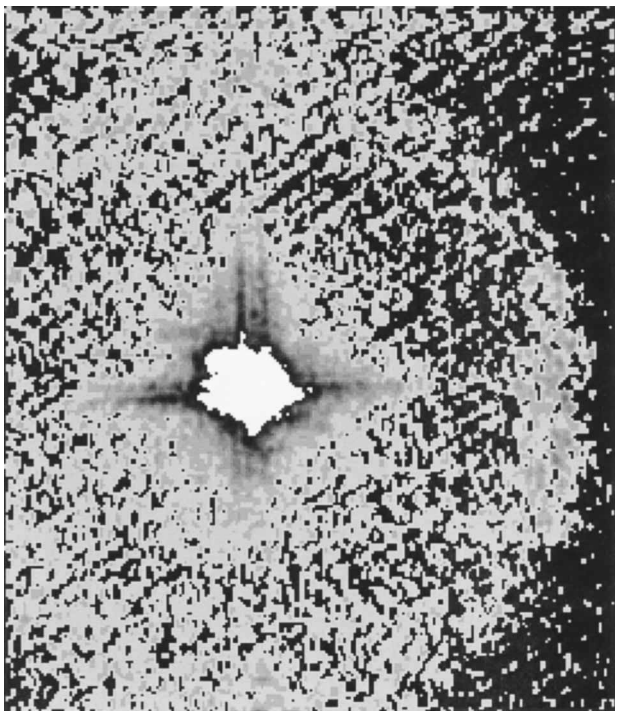

Fig. 18. Far-field image of the 1.05-μm output beam for a 5.5-GW/cm^2 shot at a 200-ps pulse width. The circular outline of the transport spatial filter pinhole can be detected at the edge of the image. The image is overexposed to enhance the wings of the spot.

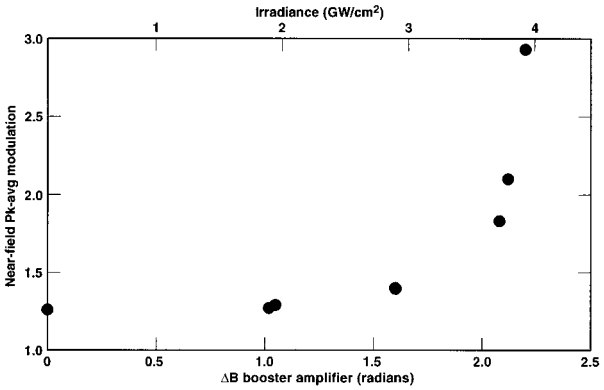

Fig. 19. Beam modulation of short pulses propagating through the unpumped booster amplifier grows rapidly as a function of the nonlinear phase shift (B integral) in the final amplifier section of the Beamlet. This modulation is representative of the last time slice of a long saturating pulse propagating through the amplifier chain under normal operation. The rapid growth of beam modulation for ΔB greater than 2 rad is apparent.

Table 3. Typical Magnitude, Scale Size, and Time Constants for Important Wave-Front Aberration Sources in a Large Glass Laser System

Aberration Source	Magnitude of Error (Peak-to-Valley Waves)[a]	Spatial Scale (Fraction of Aperture d)[b]	Time Constant for Change
Optical figure error	~λ/10–λ/4 per component, 2.5 λ cumulative	$d/4$	Static
Prompt pump-induced distortion in laser slabs	~λ/20–λ/10 per slab, ~2–3 λ cumulative	$d/4$	50 μs
Long-term residual thermal distortions	2–6 λ cumulative	$d/3$	4 h
Thermal convection currents	0.5–1 λ	$d/3$–$d/10$	seconds
Small-scale noise in optical components	λ/100–λ/50	<1–2 cm	Static

[a]Magnitude is expressed as a peak-to-valley wave-front aberration (waves at 1.05 μm).
[b]d is beam size, typically 34 cm for the Beamlet.

tions in the laser slabs. The ends of a Brewster-angle laser slab are closer to the flash lamps on one side than on the other. The side of the slab closest to the flash lamps is heated more during the pump pulse, although the total pump power to a unit area of the slab from both flash-lamp arrays taken together is constant across the aperture. The heated glass expands, bending the slab and inducing a small amount of cylinder on the beam. The cumulative effect of this distortion can amount to several waves of aberration when added over many slab passes.

A major contributor to aberrations is the residual heat deposited in the amplifiers during a shot. During the amplifier firing, the edge claddings around the glass slab that absorb amplified spontaneous emission are heated ~5–10 K, the bulk of the slab is heated ~1 K, and the flash lamps are heated ~10–15 K. This leads to several waves of thermally induced optical distortion that persist for several hours after the laser shot. Complete recovery can take more than 8 h, which is slower than the desired shot rate.

The temperature gradients in the amplifier also drive convection currents in the gas in the amplifiers and beam tubes, and the refractive-index variations caused by these currents distort the beam. These convection currents persist for several hours and change noticeably on a time scale of several seconds.

Finally, wave-front errors are produced by small-scale figure errors and other structures in the optical components. Examples are the machining marks on the KDP and residuals from small-tool figuring of laser slabs, as discussed above.

The Beamlet has an adaptive optics system[20] to correct low-spatial-frequency wave-front errors in the optical train, which gives both smaller focal spots and an increased shot rate. Figure 20 shows the deformable mirror, which is mounted after the preamplifier just before the beam is injected into the main laser cavity. The mirror has 39 electrostrictive actuators spaced on a triangular grid with 11-mm interactuator spacing and a maximum stroke of ~10 μm. The interactuator spacing that sets the scale of the wave-front errors that can be corrected corresponds to 7 cm on the output beam. A Hartmann sensor in the 1.053-μm output diagnostics package of the laser system records the wave-front distortion of a cw or pulsed alignment beam and controls the mirror in a closed loop to minimize the wave-front distortion. For the data presented here the mirror was frozen in position several minutes before each shot. The system corrects static and long-term thermal distortions when operated in this mode. Prompt pump-induced distortions can be partially corrected open-loop by recording those distortions on a reference shot and then adding the appropriate actuator displacements to the static aberrations at the time of the shot. Distortions that are due to thermal convection were not corrected in the data presented here. The control system is currently being modified to keep the feedback loop closed until 1 s before the laser shot, which will provide some correction of the convective distortions.

Figure 21 shows the far-field distribution of the Beamlet laser in the nominal far-field plane when the DFM is set to correct only static aberrations in the system, that is, with no pump-induced correction applied. A circle with a radius of 35 μrad in this plane encloses ~95% of the energy in the spot.

Figure 22 shows the far-field distribution with

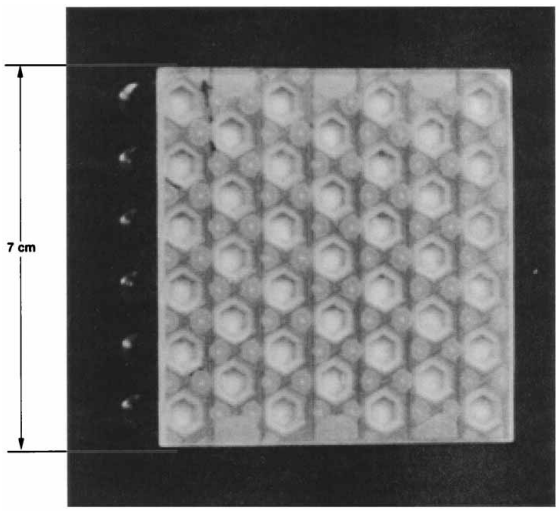

Fig. 20. The Beamlet deformable mirror has 39 actuators mounted to the back of a 7.0 cm × 7.0 cm × 0.4 cm coated fused-silica substrate. The range of motion of individual actuators is approximately 10 μm.

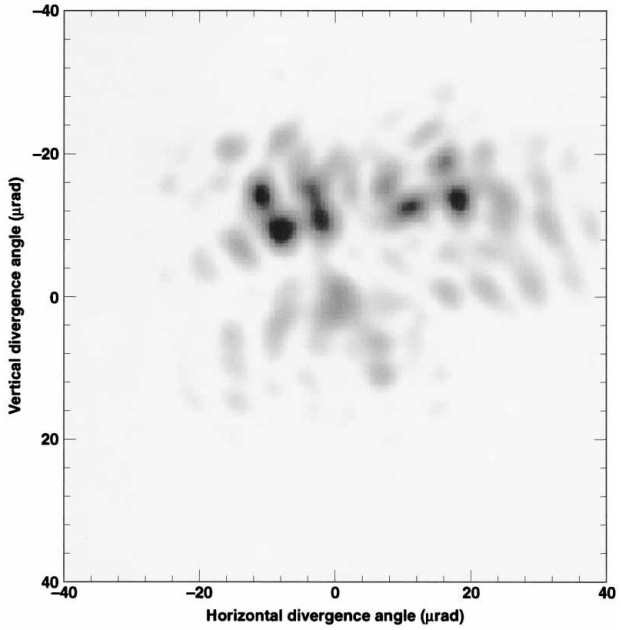

Fig. 21. Far-field irradiance distribution of the 1.05-μm beam when the adaptive optic system corrects for only static optical wave-front aberrations in the system.

static correction up to a few minutes before the shot and precorrection of the quadratic part of the pump-induced wave front. This quadratic part is partially caused by pump-induced aberration in the 5-cm-diameter cylindrical rod preamplifier. The prompt pump-induced aberration of the amplifier slabs is clearly present and in close agreement with off-line beam-steering characterization of a five-slab section.

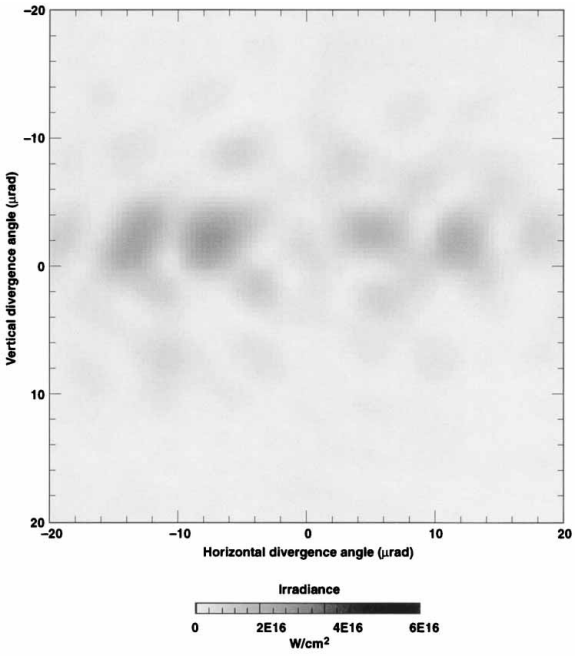

Fig. 22. Far-field irradiance distribution of the 1.05-μm beam for a shot with correction for static and power (focus) wave-front aberrations in the beam optical path.

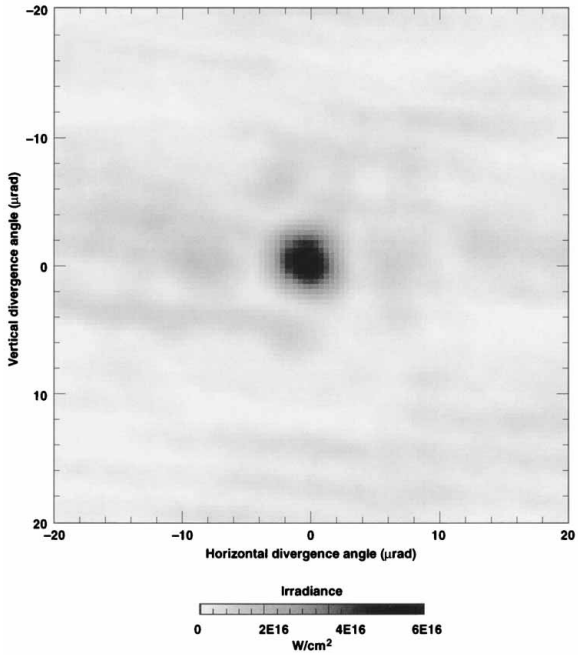

Fig. 23. Far-field irradiance distribution of the 1.05-μm beam for a shot with full precorrection for static and dynamic (flash-lamp pump-induced) phase-front aberrations.

This wave-front error has a W shape and tends to steer the beam into four distinct spots along the long axis of the slabs. Figure 23 shows the far-field distribution when an open-loop precorrection for the complete pump-induced aberration is added to the DFM actuator displacements.

Figure 24 is a more quantitative presentation of the far-field distribution of Fig. 23, showing the cumulative energy contained within a circle of a given radius in the far field. The central lobe is the size of the central lobe of the Airy pattern of the laser aperture and contains 33% of the laser energy at a Strehl

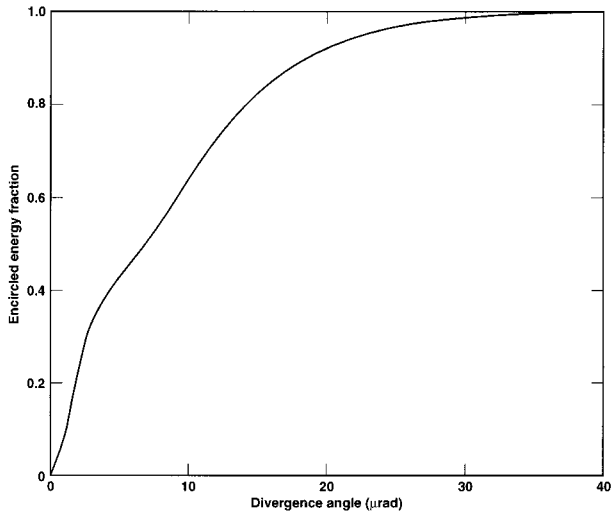

Fig. 24. Encircled energy fraction versus divergence angle determined by radial integration of the far-field irradiance distribution shown in Fig. 23.

ratio of 0.4 (a perfect plane wave would contain 84%), consistent with the shot wave-front error of 0.18 λ rms at 1.053 μm. Small-angle scattering caused by residual aberrations, outside the spatial resolution of the DFM, contribute to the pedestal around the main spot. This broadens the distribution of the remainder of the far-field energy so that 90% of the energy is enclosed in a circle whose radius corresponds to a divergence angle of 19 μrad. This shot was taken after the amplifiers had cooled for 12 h, so there was little convection. Shots taken after a cooling time of 2 h are affected by convection, and the far-field distribution degrades by a factor of ~2 after the third or fourth shot. We expect this to be partially corrected when the delay between the last DFM update and the shot is reduced to 1 s.

The correction for the thermal distortion in the amplifiers is ~4–5 waves immediately after a shot and decays to 2–3 waves after a 2-h interval. The correction increases with further shots, and limits us to 5 shots at 2-h intervals during an operating day if good beam quality must be preserved in the system. If the DFM were not present, the shot interval would have to be increased to ~8 h to maintain good beam quality on each shot.

G. Optical Damage at 1.05 μm

Over the past year, we have seen a few minor (<~1 mm) damage features appear on the large polarizer in the cavity and on the KDP Pockels cell crystal. These do not grow in size and are not a problem for operation. Lenses L_1 and L_3 have been damaged on the inside (vacuum) surface. A damaged lens, L_3, was left in place for a series of 35 high-energy shots. The damage in the thin lens grew with successive shots and caused the lens to fracture.[33] We believe that the damage threshold of these lenses was lowered by contamination from some volatile organic material such as lubricants inadvertently left on motorized components inside the vacuum. As further evidence of such contamination, the reflectivity of the solgel AR-coated lens surfaces exposed to the vacuum slowly increased from <0.5% to 2–3%, indicating that the porous solgel layer was accumulating volatile contaminants that increased the refractive index of the layer. The lenses and spatial filter hardware were thoroughly cleaned, and the new solgel coatings did not show any further degradation. We recently fired 18 high-energy shots (12 J/cm^2 at 3 ns) through the replacement lenses with no evidence of damage.

6. Harmonic Generation Experiments

A. Description of the Frequency-Conversion System

We generate the third harmonic on the Beamlet by sequential collinear sum-frequency mixing in two nonlinear optical crystals, as shown schematically in Fig. 25. A beam at the fundamental laser frequency is incident upon the first nonlinear crystal (the doubling crystal) in which second-harmonic generation takes place by means of degenerate sum-frequency mixing ($\omega_2 = \omega_1 + \omega_1$). Two copropagating beams, one at the fundamental and the other at the second harmonic, emerge from the doubling crystal. They are incident upon the second nonlinear crystal (the tripling crystal) in which the fundamental and the second harmonic again interact through sum-frequency mixing to create a wave at the third harmonic ($\omega_3 = \omega_1 + \omega_2$).

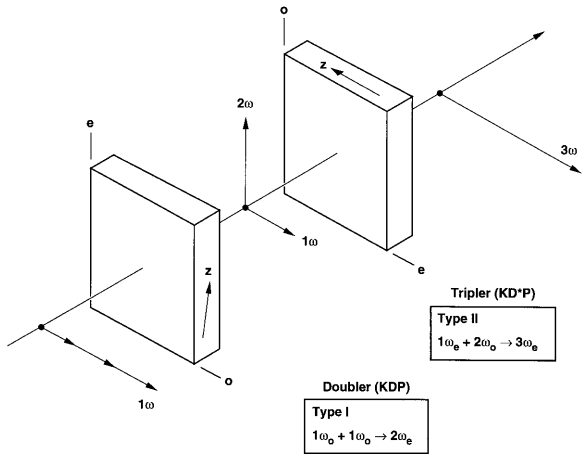

Fig. 25. Type I (KDP)/type II(KD*P) frequency-tripling scheme used on the Beamlet.

The efficiency with which power is transferred from the incident waves to the generated harmonic wave is dependent on a number of parameters, of which phase-mismatch and photon-flux balance (mix ratio) are particularly important. Phase mismatch is the difference between the **k** vector of the output harmonic and the sum of the **k** vectors of the input waves. Maximum power-transfer efficiency is attained when phase mismatch is zero and the photon fluxes of the input waves are equal. Zero phase mismatch, or phase matching, is usually achieved in nonlinear optical crystals when the birefringence of the crystal is used to balance the effects of normal dispersion. Two methods of phase matching are possible in such crystals: type I, in which the two input waves have the same polarization, and type II, in which the two input waves have orthogonal polarizations. For the Beamlet we chose a frequency-converter design consisting of type I second-harmonic generation followed by type II third-harmonic-generation.[34] Details of the harmonic generation process are described elsewhere.[35–38]

The efficiency with which the third harmonic is generated is sensitive to the ratio of the photon fluxes, or irradiances, of the fundamental and the second-harmonic beams incident upon the tripler. For the type I/type II frequency-tripling scheme used on the Beamlet, this mix ratio is controlled by the length of the doubling crystal and a slight phase mismatch created when the crystal is angularly tuned so that the beam does not propagate along the exact phase-matching direction inside the doubling crystal.

The Beamlet frequency-conversion system was designed to hold two different sizes of square crystal

plates (32 and 37 cm). These crystals can accommodate maximum beam sizes up to 30 and 34.5 cm, respectively. We activated the frequency converter with 32-cm crystals, and in later experiments we installed 37-cm crystals. The crystals and their mounts are contained within an insulated housing that limits temperature variations within ± 0.03 K, limits the relative humidity to no more than 35%, and provides cleanliness levels better than class 10. We align the crystals to an accuracy of ~ 15 μrad by measuring the location of the backreflection of the alignment beam at the transport spatial filter focal plane.

The input and the output faces of the doubling crystal are coated with a two-layer AR coating. The bottom layer is a surface-passivating silicone coating whose index of refraction is nearly the same as that of the KDP crystal. A single-layer, quarter-wave-thick, SiO_2 solgel AR coating is then placed on top of the silicone layer.[39] To simplify the crystal AR-coating process, both the input and the output faces of the doubler have an AR coating with optimum transmission at 700 nm. This provides a good compromise for optimal transmission at both 1054 and 527 nm when a single-layer AR coating is used. The output face of the tripler has a single solgel layer whose thickness is optimized for maximum transmission at 351 nm, while the input face of the tripler has an additional solgel layer applied to produce the coating thickness that optimizes transmission at 700 nm. There is no silicone coating applied to the KD*P tripler because the curing temperature of the silicone coating is greater than the phase-transition temperature of the KD*P crystal.

The tripling crystals are fabricated from 80% deuterated KD*P to reduce the potential for damage from stimulated Raman scattering (SRS). The intense Raman band that occurs in KDP near 915 cm^{-1} is split into two weaker bands in KD*P.[40,41] In addition to using KD*P, we also beveled and AR coated the edges of the crystal to prevent parasitic oscillations from SRS within the plane of the crystal and orthogonal to the beam-propagation direction.

B. Second-Harmonic Generation at 30 cm

The frequency-conversion system was activated in two stages. The 32 cm × 32 cm × 1.05 cm thick type I doubling crystal was installed first, and the second-harmonic conversion efficiency was measured as a function of input irradiance at the phase-matching angle ($\Delta k = 0$). Experiments were carried out with increasing 1ω input irradiances up to ~ 5.3 GW/cm^2 by use of 1-ns square pulses. The second-harmonic conversion efficiency increased monotonically with drive irradiance, reaching a maximum value of 83%. This efficiency, and all other efficiencies quoted for this section, is whole-beam energy conversion, including all spatial and temporal structures on the beam. The results for the 32-cm crystals are shown in Fig. 26 and are found to be in excellent agreement with plane-wave model calculations. This attests to the low wave-front distortion of the Beamlet 1ω drive beam.

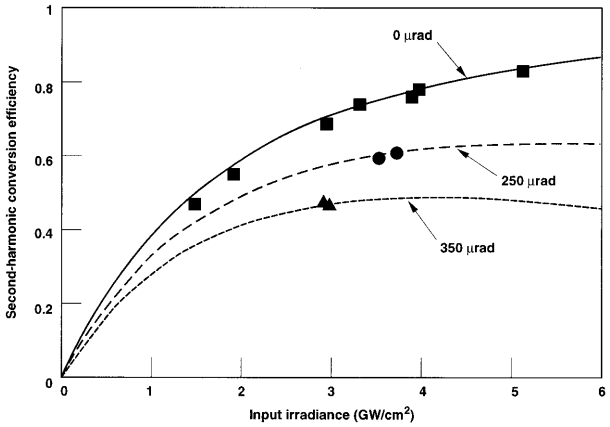

Fig. 26. Second-harmonic conversion efficiency versus 1ω drive irradiance with a 32 cm × 32 cm × 1.1 cm KDP type I doubling crystal. The conversion efficiency agrees with the plane-wave model at 0-, ±250-, and ±350-μrad detuning angles.

The plane-wave model assumes a 1% loss at each AR-coated surface of the crystals and 6%/cm absorption at 1054 nm by the bulk KDP.[28] As noted above in this section, the second-harmonic generation crystal is slightly detuned from the phase-matching angle to achieve the proper mix ratio of the fundamental and second-harmonic beam that drives the tripler. Calculations predict that a detuning angle of ±250 μrad from the phase-matching direction in the crystal will give the correct mix ratio to achieve maximum third-harmonic conversion at incident fundamental irradiances between 3 and 4 GW/cm^2.

During the course of the second-harmonic generation experiments, we also measured the conversion efficiency at detuning angles of ±250 and ±350 μrad and compared the results with the plane-wave model (Fig. 26). Again, the agreement between the model and experiment was very good. To perform these conversion tests, the doubling crystal was first tilted (detuned) in one direction away from the phase-matching direction and the conversion efficiency measured. This experiment was then repeated with the crystal tilted an equivalent amount in the opposite direction. Thus the two points shown in Fig. 26 at each of the detuning angles represent two separate experiments in which the crystal was detuned by an equal amount in opposite directions from the exact phase-matching angle.

C. Third-Harmonic Generation at 30 cm

Table 4 summarizes the results from third-harmonic generation experiments carried out with a 3-ns square-pulse shape, and these results are compared with the NIF 351-nm performance requirements. There are three key third-harmonic performance criteria the Beamlet must meet: (1) fluence, (2) beam quality, and (3) conversion efficiency. Perhaps the most critical performance criteria is the 3ω fluence, because of the lower optical-damage limits at shorter

Table 4. Summary of Beamlet Third-Harmonic Performance Parameters

Parameter	Beamlet			NIF Design Requirements
	Design Requirement	32-cm crystals	37-cm crystals	
Mean 3ω fluence (J/cm^2)	6.4–7.6	8.7	8.2	8.0
Beam size (cm^2)	30 × 30	29.6 × 29.6	34 × 34	38 × 38
Effective beam area (cm^2)	784	736	1017	1300
3ω energy (kJ)	5–6	6.4	8.3	10.2
Beam divergence (μrad)	≤±50	≤±25	≤±25	≤±35
Bandwidth (GHz)	90	90	90	90

wavelengths (see Table 1). Specifically, the optical material most at risk is the tripling crystal, because the laser output is set to be near the damage threshold of this material. During the tests with 32-cm crystals, we carried out 17 shots with fluences exceeding 7.5 J/cm^2 at 3 ns without sustaining any significant damage to the KD*P tripling crystal.

We activated the third-harmonic converter by first laser conditioning the KD*P tripling crystal at 3ω. Laser conditioning refers to the process of increasing the damage threshold of an optical material by exposing it to a series of laser shots with monotonically increasing fluence.[23] Following conditioning, a series of experiments was conducted to characterize the 3ω conversion performance. One of our major goals was to demonstrate >70% conversion efficiency at high peak power (2.5–3.5 GW/cm^2). These experiments were carried out with temporally square, 3-ns pulses. Figure 27 shows the measured the third-harmonic conversion efficiency plotted versus the 1ω input irradiance delivered to the harmonic converter system. At the highest drive irradiances (>3.25 GW/cm^2), conversion efficiencies of 80% were achieved. Also shown in Fig. 27 are plane-wave model predictions. The model calculations include the effects of the 30-GHz bandwidth (90 GHz at the 3ω output) that we add to the input drive pulse to suppress transverse SBS in the output optics. The added bandwidth reduces the conversion efficiency ~3% at the highest drive irradiances. The model calculation shown in Fig. 27 does not include the effects of the spatial and the temporal edges of the real beam, but instead assumes a perfect top-hat-shaped profile. Including these effects would tend to reduce the conversion efficiency slightly, giving even closer agreement with the experiments. The maximum average 3ω output fluence achieved during this series of shots was 8.7 J/cm^2 at the Beamlet nominal 30-cm beam-aperture area of 736 cm^2, which gave a 3ω output energy of 6.4 kJ (Table 4).

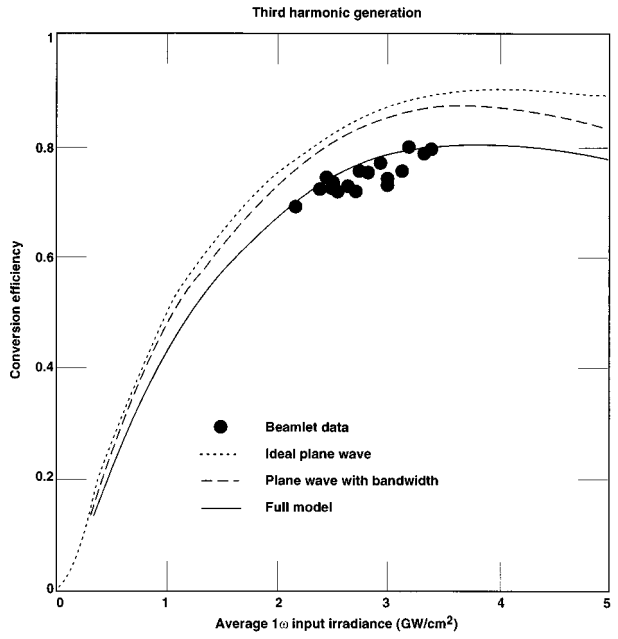

Fig. 27. Third-harmonic conversion efficiency versus 1ω drive irradiance achieved with 3-ns square pulses with 30-GHz 1ω bandwidth (90 GHz at 3ω). The type II tripling crystal was 80% deuterated KD*P 32 cm × 32 cm × 0.95 cm with 0-μrad detuning. The doubling crystal was detuned at ~250 μrad to achieve optimum 3ω conversion.

The input beam quality and fill factor were maintained during the third-harmonic generation process, as shown by the 3ω near-field image and line-out in Fig. 28. These data were taken during a 3-ns shot at an input drive irradiance of 2.6 GW/cm^2, which produced 7.7-J/cm^2 (5.6-kJ) output at 3ω. The peak-to-mean fluence modulation is ~1.4:1 at 3ω compared with ~1.3:1 at 1ω. Figure 29 further illustrates the similarity in the fluence modulation observed for the 1ω and 3ω near-field images at high drive irradiances. Shown in the plot is the normalized probability distribution of fluences observed at 1ω and 3ω for a 3-ns shot. The average pulse irradiances are 3.3 and 2.7 GW/cm^2 at 1ω and 3ω, respectively. The wings of the two curves compare the peak-to-valley irradiance distribution for the 1ω and 3ω pulses. The data clearly show that there is no significant growth in near-field fluence modulation during the conversion process. Another measure of the quality of the output beam is its focusability. Displayed in Fig. 30 is a plot of the energy content versus far-field divergence angle obtained from a radial integration of the far-field irradiance profiles of the fundamental beam incident upon the frequency converter and the output third-harmonic beam. These data were taken at a 1ω irradiance of 2.1 GW/cm^2 and a 3ω irradiance of 1.4 GW/cm^2 at a pulse length of 3 ns.

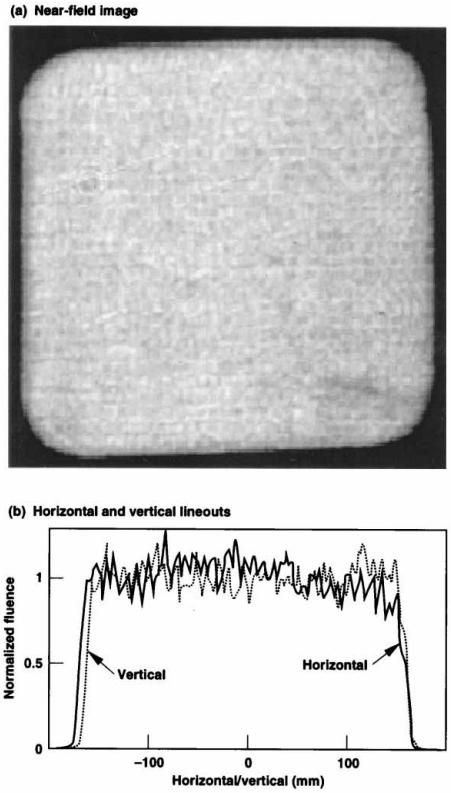

Fig. 28. (a) Near-field image, (b) horizontal and vertical fluence line-outs of that image of a 351-nm output pulse from the Beamlet harmonic generator. The peak-to-mean irradiance modulation is ~1.35 to 1.

During the course of our third-harmonic generation tests with the 32-cm crystals, we also demonstrated frequency conversion for shaped pulses roughly similar to NIF ignition target drive pulses. The proposed NIF ignition target pulse shape consists of a low-irradiance foot ~15 ns long followed by a higher irradiance, 3–3.5-ns, main drive pulse. The harmonic generation process depends strongly on the product of the beam irradiance and crystal thickness

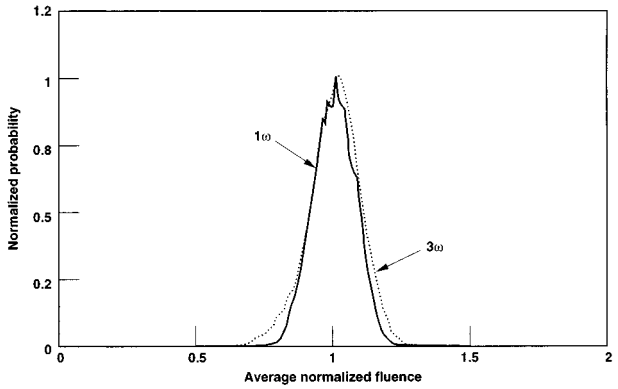

Fig. 29. Comparison of normalized probability distribution of fluences for the 1ω drive pulse with corresponding 351-nm output observed during a 3-ns shot at a 1ω input drive irradiance of 3.3 GW/cm^2.

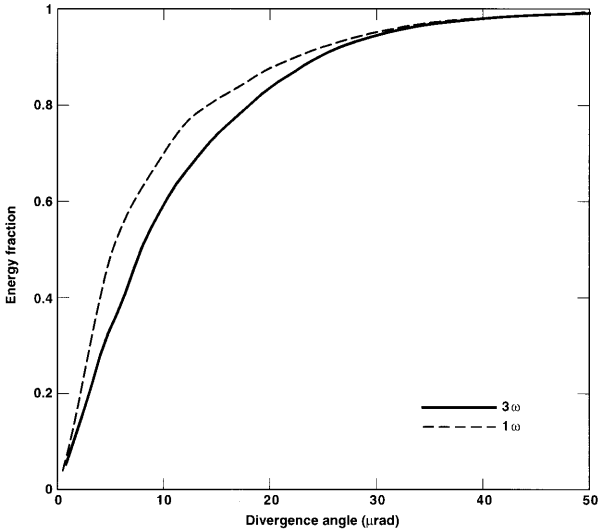

Fig. 30. Encircled energy fraction versus divergence angle determined by radial integration of the 1ω and 3ω far-field irradiance distributions.

and therefore has a limited irradiance range over which it is fully optimized. The crystal thicknesses used on the Beamlet were chosen to optimize conversion efficiency for drive irradiances of 2–5 GW/cm^2. This is illustrated by the data in Fig. 27, in which the conversion efficiency is shown to drop off dramatically at low drive irradiance. In both the NIF and the prototypical Beamlet design, the conversion efficiency of the foot will be significantly lower than the main pulse. The NIF requirement is 60% conversion efficiency for the nominal ignition pulse shape. Because the Beamlet preamplifier section was designed to handle a maximum pulse length of 10 ns, we simulated a complex pulse shape (similar to what might be used at the NIF) by using a 7-ns foot and a 3-ns main pulse. The 1ω input to the harmonic converter had a foot-to-main-pulse contrast ratio of 9:1, giving the desired 30:1 contrast ratio for the 3ω output pulse (Fig. 31). The 1ω beam had an equivalent pulse length of 3.9 ns and a mean fluence of 12.4 J/cm^2 compared with 3.2 ns and 8.2 J/cm^2 for the output 3ω pulse. The measured foot and peak pulse third-harmonic conversion efficiencies were 23% and 77%, respectively. The average tripling efficiency was 64%, which compares quite favorably with our model predictions.

The shaped-pulse experiments described above also gave us the added opportunity to test more fully the capability of the integrated optical-pulse-forming and preamplifier section of our front end. To create the desired 9:1 1ω NIF-like pulse shape that was used to drive the harmonic converter requires nearly a 75:1 irradiance contrast for the shaped pulse at the injection to the main laser cavity (Fig. 32).

D. Harmonic Generation at 34 cm

A second set of harmonic generation experiments was performed with the 37 cm × 37 cm KDP frequency-

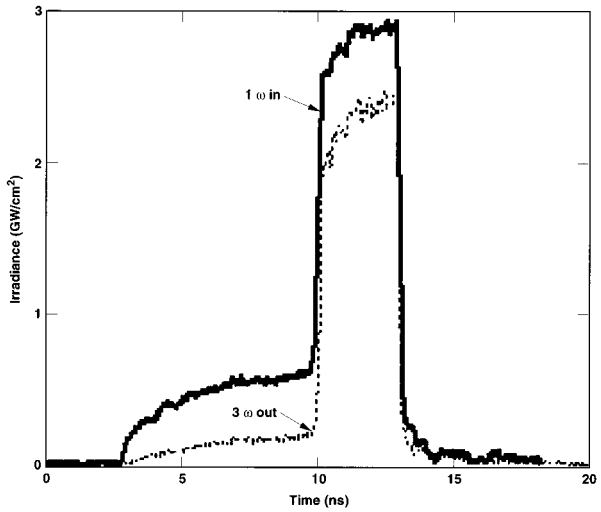

Fig. 31. Simulated NIF-like 3ω temporal pulse shape with a 30:1 irradiance contrast ratio generated with a 9:1 1ω drive pulse to the harmonic converter. The foot of the actual NIF pulse is 15 ns long rather than 7 ns, as used in this experiment.

conversion crystals at a beam size of 34 cm × 34 cm. As we did with the 32-cm crystals, we activated the doubling crystal first with a short series of second-harmonic generation experiments. We then installed and aligned the tripling crystal, activating it with a series of shots of increasing fluence in order to laser condition the KDP crystals. Shown in Fig. 33 is a plot of output third-harmonic energy versus input energy at the fundamental for pulse lengths of 1, 1.7, and 3 ns. This series of shots culminated in an output third-harmonic energy of 8.3 kJ at an average fluence of 8.2 J/cm^2. The maximum third-harmonic

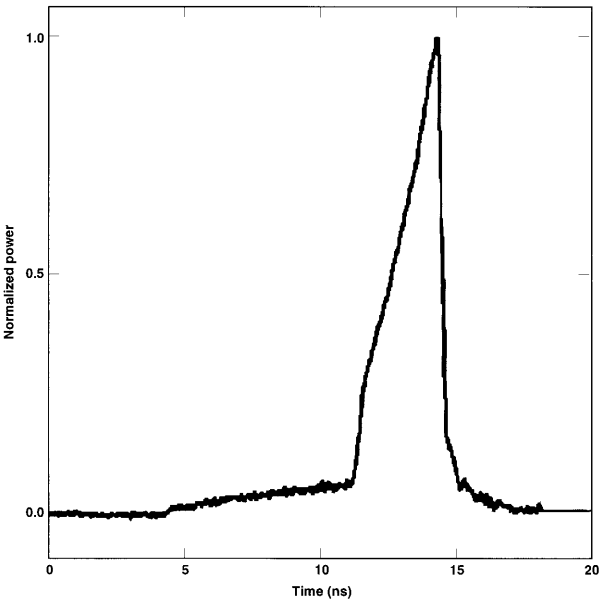

Fig. 32. Input 1ω pulse shape (injected into the main multipass cavity) with a 75:1 irradiance contrast and a complex temporal shape needed to achieve the desired 1ω output pulse shape to the frequency converter (see Fig. 31).

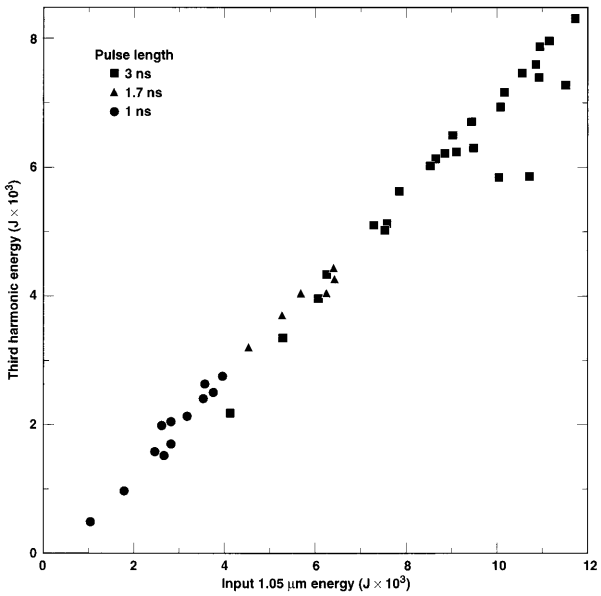

Fig. 33. Third-harmonic output energy versus 1ω input energy. The data were recorded at pulse lengths of 1, 1.7, and 3 ns with the 37-cm crystals. The four outlying points at 3 ns are shots deliberately detuned to verify alignment.

conversion efficiency observed during this shot campaign was 72%. At least part of the reduction in conversion efficiency from that observed during the 32-cm frequency converter experiments appears to be attributable to slightly poorer quality of the larger crystals and crystal mounts that warp the larger crystals, which leads to increased wave-front aberration inside the crystals and degrades our ability to align them accurately.

During this series of shots, we also studied transverse SRS in the tripling crystal. Optical fibers positioned along the edges of the tripling crystal allowed us to collect and spectrally analyze the light scattered from the tripler. Although we saw significant nonlinear growth of the 881-cm^{-1} Raman mode of 80% deuterated KDP, no damage to the tripler crystal or the absorbing glass surrounding it was observed. The value of the SRS gain coefficient we measured was 0.098 cm/GW, which is in good agreement with the expected value of 0.11 cm/GW calculated from other measurements. The details of these transverse SRS studies are reported elsewhere.[34,40]

E. Optical Damage at 351 nm

Optical damage thresholds at 351 nm are significantly less than at 1053 nm and will ultimately limit the output fluence of the laser. The Beamlet has three optics that are exposed to high-fluence 351-nm light: the KD*P tripler crystal, a high-quality fused-silica 3ω diagnostic splitter, and a low-quality negative lens (see Fig. 5). The beam splitter and the negative lens are located 1 and 3 m downstream from the tripler crystal, respectively. During the har-

monic conversion tests we carefully monitored damage to these three optics.

At the completion of the 32-cm tests, the tripler crystal showed no observable damage and the diagnostic splitter showed only a few minor (millimeter size) damage spots. The negative lens showed somewhat more damage and also several self-focusing tracks; this level of damage is consistent with the lower-quality optical finish and material that was used for this noncritical optic.

The damage observed during the test with the 37-cm crystals was roughly comparable with that observed with the 32-cm crystals. The only exception is that the negative lens suffered more surface damage and self-focusing tracks than were observed with the 32-cm crystals. We attribute this increased damage with the 37-cm crystals to irradiance modulation that develops with downstream propagation of the beam. This is caused by phase and irradiance modulation imposed on the beam by the lower optical quality and diamond-turning marks of the 37-cm crystals.

7. Progression from the Beamlet, as Configured for these Tests, to the NIF Design

As mentioned above, the NIF laser design[1] has some small differences from the Beamlet configuration reported in this paper, although the concepts and the operating fluences are the same. We expect that there will be additional minor changes to the NIF design before it is frozen, based on Beamlet tests and other results. These differences are the result of continuing design and cost studies since the time that the Beamlet hardware design was frozen in early 1991, as well as some limitations on the size of crystals available for these early Beamlet tests. We describe these differences here.

With short laser pulses, the output power from the Beamlet laser is limited by the growth of amplitude noise caused by the nonlinear phase shift on the last pass through the Pockels cell and the five-slab-long booster amplifier. For long pulses the limit is set by the nonlinear phase shift in the last round trip through the 11-slab-long multipass main amplifier. A typical operating limit is 2 rad of nonlinear phase shift at the average irradiance of the profile at the end of the laser pulse for either of these propagation paths.[17,18] The 11 and 5 distributions of the Beamlet amplifier slabs place the crossover point between these two nonlinear phase-shift limits at a pulse length of ~3 ns and optimize performances for pulses of roughly that duration. For pulses longer than ~8–10 ns, the output fluence reaches a limit set by the stored fluence in the amplifier and the optical losses in the system. The NIF will be configured for optimum performance at slightly longer pulses of ~5 ns, so the two amplifiers will contain 11 and 7 slabs rather than 11 and 5. The amplifier slabs in the NIF design[1] have a slightly larger clear aperture (40 versus 39 cm) than the Beamlet slabs, and the flashlamp pump pulse is shorter. This gives somewhat higher storage efficiency and lower cost, as discussed in other publications.[1,7] The NIF slabs will use a slightly different glass composition that is easier to manufacture. Slabs of that composition will be tested on the Beamlet in the coming year.

The beam dimensions for the NIF design[1] are 38 cm × 38 cm at the zero-irradiance point rather than the 30–35-cm^2 beams demonstrated in this Beamlet test series. These larger dimensions are the result of a larger clear aperture in the switch crystal and amplifier, smaller separations between pinholes in the spatial filters, and different vignetting allowances in the slightly longer cavity of the NIF design.

The input pulse to the main laser cavity for the NIF will be injected into the transport spatial filter rather than the cavity spatial filter (see Fig. 3). This gives one additional pass through the booster amplifier, reducing the size of the front end. Also, the NIF transport spatial filter is much longer than the cavity spatial filter, allowing a smaller off-axis angle for the same size of beam-injection hardware.

8. Future Studies on the Beamlet

The tests of the Beamlet laser reported here show that the laser architecture and performance proposed for the NIF can be realized in practice. Over the next several years, the Beamlet will be used as a testbed for further developments of laser technology for the NIF. A vacuum chamber has been installed at the laser output to measure the spatial intensity profile of the 3ω target irradiation spot and the performance of a prototype final optics assembly. Long-term changes in the optical components will be monitored, and the new laser glass composition will be tested. Prototypes of alignment and diagnostics systems and some variations in laser architecture will be explored. The performance under all these conditions will be carefully compared with computer simulations to validate the accuracy of these models.

We gratefully acknowledge the contributions of the many Lawrence Livermore National Laboratory engineers, technicians, scientists, and support personnel whose efforts made this project possible; where possible the contributions of these individuals are recognized through references to their publications on specific Beamlet components. We also appreciate the high-quality, state-of-the-art optical, electrical, and mechanical components delivered by numerous vendors, particularly Aerovox, Cleveland Crystals, Corning, Eastman Kodak Company, EG&G, Maxwell Laboratories, Passat Enterprises, Schott Glass Technologies, Spectra-Physics, Tinsley Laboratories, United Technologies, and Zygo. This research is supported by the U.S. Department of Energy (DOE) under contract W-7405-ENG-48 and by the Comissariat a l'Energie Atomique (CEA) of France through a joint DOE/CEA cooperative research agreement.

References

1. "National Ignition Facility Conceptual Design Report," UCRL-PROP-117093 (May 1994) Available from the National Tech-

nical Information Service (NTIS), U.S. Dept. of Commerce, 5285 Port Royal Rd., Springfield, Va. 22161; J. A. Paisner, J. D. Boyes, S. A. Kumpan, W. H. Lowdermilk, and M. S. Sorem, "Conceptual design of the National Ignition Facility," in *Solid State Lasers for Application to Inertial Confinement Fusion,* M. André and H. T. Powell, eds., Proc. SPIE **2633,** 2–12 (1995).
2. M. Andre, M. Novaro, and D. Schirmann, "Technologie pour un laser megajoules," Rev. Sci. Tech. Direction Appl. Militaires **13,** 73–84 (1995).
3. J. Lindl, "Development of the indirect-drive approach to inertial confinement fusion and the target physics basis for ignition and gain," Phys. Plasmas **2,** 3933–4024 (1995).
4. B. M. Van Wonterghem, D. R. Speck, M. J. Norman, V. Karpenko, and R. B. Wilcox, "The Beamlet front end: prototype of a new pulse generation subsystem," Lawrence Livermore National Laboratory Rep. UCRL-LR-105821-93-1, ICF Quarterly Report **3**(1), 9 (1993). Available from NTIS; see Ref. 1.
5. M. A. Rhodes, B. Woods, J. J. DeYoreo, D. Roberts, and L. J. Atherton, "Performance of large-aperture optical switches for high-energy ICF lasers," Appl. Opt. **34,** 5313–5330 (1995).
6. J. Goldhar and M. A. Henesian, "Large-aperture electrooptical switches with plasma electrodes," IEEE J. Quantum Electron. **QE-22,** 1137–1147 (1986).
7. A. C. Erlandson, M. D. Rotter, K. S. Jancaitis, D. N. Frank, and R. W. McCracken, "Design and performance of the Beamlet amplifiers," Lawrence Livermore National Laboratory Rep. UCRL-LR-105821-95-1, ICF Quarterly Report **5**(1), 18–28 (1995); M. D. Rotter, R. W. McCracken, A. C. Erlandson, and D. W. Brown, "Thermal recovery measurements on multisegment amplifers," in *Solid State Lasers for Application to Inertial Confinement Fusion,* M. André and H. T. Powell, eds., Proc. SPIE **2633,** 70–81 (1995).
8. D. Larson, "Beamlet pulsed-power system," Lawrence Livermore National Laboratory Rep. UCRL-LR-105821-95-1, ICF Quarterly Report **5**(1), 62–67 (1995). Available from NTIS; see Ref. 1.
9. S. Seznec, C. S. Vann, F. Laniesse, J. E. Murray, H. G. Patton, and B. M. Van Wonterghem, "Testing a new laser architecture concept on Beamlet," Lawrence Livermore National Laboratory Rep. UCRL-LR-105821-95-2, ICF Quarterly Report **5**(2), 142–150 (1995). Available from NTIS; see Ref. 1.
10. J. T. Hunt and D. R. Speck, "Present and future performance of the Nova laser system," Opt. Eng. **28,** 461–468 (1989).
11. W. W. Simmons and R. O. Godwin, "Nova laser fusion facility—design, engineering and assembly overview," Nucl. Technol. Fusion **4,** 8–24 (1983).
12. C. Bibeau, D. R. Speck, R. B. Ehrlich, C. W. Laumann, D. T. Kyrazis, M. A. Henesian, J. K. Lawson, M. D. Perry, P. J. Wegner, and T. L. Weiland, "Power, energy, and temporal performance of the Nova laser facility with recent improvements to the amplifier system," Appl. Opt. **31,** 5799–5808 (1992).
13. T. R. Boehly, R. S. Craxton, T. H. Hinterman, P. A. Jaanimagi, J. H. Kelly, T. J. Kesselr, R. L. Kremens, S. A. Kumpan, S. A. Letzring, R. L. McCrory, S. F. B. Morse, W. Seka, S. Skupsky, J. M. Soures, and C. P. Verdon, "The Omega upgrade laser system," Fusion Technol. **26,** part 2, 722–729 (1994).
14. C. Yamanaka, "Inertial confinement fusion in Japan," Laser Particle Beams **2,** 425–431 (1984).
15. G. Thiell, A. Adolf, M. Andre, N. Fleurot, D. D. Juraszek, and D. Schirman, "The Phébus experimental facility operating at 250 ps and 0.53 μm," Laser Particle Beams **6,** 93–103 (1988).
16. M. J. Norman, R. M. Stevenson, I. C. Smith, D. Bowley-Booth, I. K. Pearce, and T. H. Bett, "Recent improvements to the HELEN laser system," in *Conference Proceedings of QE-9: The Ninth National Quantum Electronics Conference* (Oxford U. Press, London, 1989), p. 66.
17. J. T. Hunt, J. A. Glaze, W. W. Simmons, and P. Renard, "Suppression of self-focusing through low-pass spatial filtering and relay imaging," Appl. Opt. **17,** 2053–2057 (1978).
18. W. W. Simmons, J. T. Hunt, and W. E. Warren, "Light propagation through large laser systems," IEEE J. Quantum Electron. **QE-17,** 1727–1744 (1981).
19. S. W. Mead, R. E. Kidder, J. E. Swain, F. Rainer, and J. Petruzzi, "Preliminary measurements of x-ray and neutron emission from laser-produced plasmas," Appl. Opt. **11,** 345–352 (1972).
20. J. T. Salmon, E. S. Bliss, T. W. Long, E. L. Orham, R. W. Presta, C. D. Swift, and R. S. Ward, "Real-time wavefront correction using a zonal deformable mirror and a Hartmann sensor," in *Active and Adaptive Optical Systems*, M. A. Ealey, ed., Proc. SPIE **1542,** 459–467 (1991); J. T. Salmon, E. S. Bliss, J. L. Byrd, M. Feldman, M. W. Kartz, J. S. Toeppen, B. M. Van Wonterghem, and S. E. Winters, "Adaptive optics system for solid-state laser systems used in inertial confinement fusion," in *Solid State Lasers for Application to Inertial Confinement Fusion,* M. André and H. T. Powell, eds., Proc. SPIE **2633,** 105–115 (1995).
21. J. H. Campbell, L. J. Atherton, J. J. De Yoreo, M. R. Kozlowski, R. T. Maney, R. C. Montesanti, L. M. Sheehan, and C. B. Barker, "Large aperture, high damage threshold optics for Beamlet," Lawrence Livermore National Laboratory Rep. UCRL-LR-105821-95-1, ICF Quarterly Report **5**(1), 52–61 (1995). Available from NTIS; see Ref. 1.
22. M. R. Kozlowski, I. M. Thomas, J. H. Campbell, and F. Rainer, "High-power optical coatings for a megajoule-class ICF laser," in *Thin Films for Optical Systems*, K. H. Guenther, ed., Proc. SPIE **1782,** 105–121 (1992).
23. F. Rainer, L. J. Atherton, and J. J. De Yoreo, "Laser damage to production- and research-grade KDP crystals," in *Laser-Induced Damage in Optical Materials*, H. E. Bennett, L. L. Chase, A. H. Guenther, B. Newnam, and M. Soileau, eds., Proc. SPIE **1848,** 46–58 (1992).
24. J. M. Eggleston and M. J. Kushner, "Stimulated Brillouin scattering parasitics in large optical windows," Opt. Lett. **12,** 410–412 (1987).
25. J. R. Murray, J. Ray Smith, R. B. Ehrlich, D. T. Kyrazis, C. E. Thompson, T. L. Weiland, and R. B. Wilcox, "Experimental observation and suppression of transverse stimulated Brillouin scattering in large optical components," J. Opt. Soc. Am. B **6,** 2402–2411 (1989).
26. G. Arisholm and P. Narum, "Transient transverse stimulated Brillouin scattering with a broad-band pump," IEEE J. Quantum Electron. **28,** 2075–2083 (1992).
27. J. H. Campbell, "Recent advances in phosphate laser glasses for high power applications," in *Inorganic Optical Materials*, P. Klocek, ed., Vol. CR64 of SPIE Critical Reviews Series (Society of Photo-Optical Instrumentation Engineers, Bellingham, Wash., 1996), pp. 3–39.
28. C. A. Ebbers, J. Happe, N. Nielsen, and S. P. Velsko, "Optical absorption at 1.06 μm in highly deuterated potassium dihydrogen phosphate," Appl. Opt. **31,** 1960–1964 (1992).
29. W. Seka, S. D. Jacobs, J. E. Rizzo, R. Boni, and R. S. Craxton, "Demonstration of high-efficiency third-harmonic conversion of high-power Nd-glass laser radiation," Opt. Commun. **34,** 469–473 (1980).
30. J. M. Auerbach and V. P. Karpenko, "Serrated-aperture apodizers for high-energy laser systems," Appl. Opt. **33,** 3179–3183 (1993).
31. J. H. Campbell, F. Rainer, M. Kozlowski, C. R. Wolfe, I. M. Thomas, and F. Milanovich, "Damage resistant optics for a mega-joule solid state laser," in *Laser-Induced Damage in Optical Materials: 1990*, H. E. Bennett, L. L. Chase, A. H. Guenther, B. Newnam, and M. Soileau, eds., Proc. SPIE **1441,** 444–456 (1990).

32. J. M. Auerbach, J. K. Lawson, M. D. Rotter, B. M. Van Wonterghem, and W. H. Williams, "Performance modeling of Beamlet," in *Solid State Lasers for Application to Inertial Confinement Fusion,* M. André and H. T. Powell, eds., Proc. SPIE **2633,** 405–411 (1995).
33. J. H. Campbell, G. J. Edwards, and J. E. Marion, "Damage and fracture in large aperture, fused silica, vacuum spatial filter lenses," in *Solid State Lasers for Application to Inertial Confinement Fusion,* M. André and H. T. Powell, eds., Proc. SPIE **2633,** 522–534 (1995).
34. C. E. Barker, B. M. Van Wonterghem, J. M. Auerbach, R. J. Foley, J. R. Murray, J. H. Campbell, J. A. Caird, D. R. Speck, and B. Woods, "Design and performance of the Beamlet laser third harmonic frequency converter," in *Solid-State Lasers for Application to Inertial Confinement Fusion,* M. André and H. T. Powell, eds., Proc. SPIE **2633,** 398–404 (1995).
35. R. S. Craxton, "Theory of high-efficiency third harmonic generation of high-power Nd-glass radiation," Opt. Commun. **34,** 474–478 (1980).
36. R. S. Craxton, "High-efficiency frequency tripling schemes for high-power Nd:glass lasers," IEEE J. Quantum Electron. **QE-17,** 1771–1782 (1981).
37. P. J. Wegner, M. A. Henesian, D. R. Speck, C. Bibeau, R. B. Ehrlich, C. W. Laumann, J. K. Lawson, and T. L. Weiland, "Harmonic conversion of large-aperture 1.05-μm laser beams for inertial confinement fusion research," Appl. Opt. **31,** 6414–6426 (1992).
38. J. K. Lawson, D. R. Speck, C. Bibeau, S. C. Burkhart, M. A. Henesian, C. W. Laumann, T. L. Weiland, and R. Wilcox, "Temporal shaping of third-harmonic pulses on the Nova laser system," Appl. Opt. **31,** 5061–5068 (1992).
39. I. M. Thomas, "Optical and environmentally protective coatings for KDP harmonic converter crystals," presented at the SPIE 1991 International Symposium, San Diego, Calif., 21–26 July 1991.
40. C. E. Barker, R. A. Sacks, B. M. Van Wonterghem, J. A. Caird, J. R. Murray, J. H. Campbell, K. Kyle, R. B. Ehrlich, and N. D. Nielsen, "Transverse stimulated Raman scattering in KDP," in *Solid State Lasers for Application to Inertial Confinement Fusion*, M. André and H. T. Powell, eds., Proc. SPIE **2633,** 501–505 (1995).
41. V. N. Novikov, S. A. Bel'kov, G. G. Kochemasov, S. M. Kulikov, N. N. Rukavishnikov, S. A. Sukharev, I. N. Voronich, and A. I. Zaretskii, "Stimulated Raman scattering in frequency conversion crystals," in *Solid-State Lasers for Application to Inertial Confinement Fusion,* M. André and H. T. Powell, eds., Proc. SPIE **2633,** 506–512 (1995).